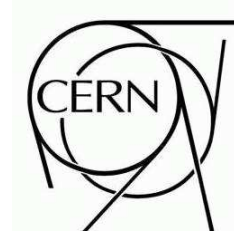


ATLAS NOTE

ATL-PHYS-PUB-2006-XXX

14th January 2008



Dileptons and Diphoton Resonances at High Masses

The ATLAS Collaboration

Abstract

The dileptons and diphotons final states are crucial for the new physics searches in the first years of the LHC running. They are the most robust channels to analyze because of the simplicity of the event topology. After studying the Standard Model predictions and understanding the uncertainties associated with them one can then look for significant deviations as an indication of beyond the Standard Model physics (BSM). While this note addresses many BSM topics, the main intent is to prepare for the first data delivered by the LHC to the ATLAS detector. In particular, this is the first note that addresses these searches including the effects of trigger requirements, misalignment, and miscalibration of the detector. Since the analysis techniques are very similar if not identical among different sources of BSM physics, we focus mostly on the final state rather than any theory in particular. We discuss the issues concerning lepton and photon reconstruction and identification, trigger efficiencies, backgrounds from physics signatures and from instrumental fakes, optimization of limit setting, as well as many theoretical uncertainties. The focus of the note is to study the prospects for discovering BSM physics in the dilepton and diphoton and final states with an assumed integrated luminosity ranging from 100 pb^{-1} to 10 fb^{-1} .

Contents

1	Introduction	4
2	Monte Carlo Samples	5
3	Object Identification and Performance	7
3.1	Electrons	7
3.1.1	Identification	7
3.1.2	Energy resolution	7
3.1.3	Charge reconstruction	8
3.1.4	Invariant mass reconstruction	8
3.1.5	Bremsstrahlung recovery	8
3.2	Muon reconstruction and identification	10
3.2.1	Performance on Monte Carlo	10
3.2.2	Efficiency from data	11
3.2.3	Extrapolation to high p_T using the tag/probe method	13
3.2.4	Charge Misidentification	13
3.2.5	Radiative Effects	14
3.2.6	Effects of Misalignment	15
3.2.7	Z' invariant mass for different misalignment hypotheses	18
3.3	Photons	21
3.3.1	Acceptance and Efficiency Determination	21
3.3.2	Isolation Optimization	23
3.3.3	Fake Rate Estimation	25
3.4	Tau Identification	26
4	Trigger Requirements	29
4.1	Introduction	29
4.2	Electron and Photon Triggers	29
4.2.1	Efficiencies and normalizations	29
4.2.2	Object based efficiencies	30
4.2.3	Event based Efficiencies	30
4.2.4	Effect of the trigger on invariant mass distributions	31
4.2.5	Current trigger configuration and strategy with early data	31
4.3	Muon Triggers	33
4.3.1	Efficiency Estimate	33
4.4	Tau Triggers	38
5	Uncertainties and backgrounds	40
5.1	Dileptons	40
5.1.1	Theoretical uncertainties	40
5.1.2	Luminosity	43
5.1.3	Summary of systematic uncertainties	45
6	Search for Exotic Physics	46
6.1	Introduction	46
6.2	$Z' \rightarrow ee$ in the parameterised fit approach	46
6.3	$G^* \rightarrow e^+e^-$ in a non-parameterised approach	52

6.4	$G \rightarrow \tau\tau$ using the number counting approach	56
6.5	$G \rightarrow \gamma\gamma$ using number counting approach	59
6.6	Technicolor using a non parameterised approach	62
A	Effect of alignment On the sensitivity to $Z' \rightarrow \mu\mu$ channel	66
	Bibliography	
	70	

1 Introduction

Many fundamental discoveries in particle physics have made searching for dilepton resonances (e.g. the J/Ψ [1, 2], Υ mesons [3] and the Z boson [4]). Dilepton and diphoton final state will be an important channel to study at the LHC during the early running. These final states are very promising due to the low background and high trigger and reconstruction efficiency. New heavy states forming a narrow resonance decaying into dileptons are predicted in many extensions of the Standard Model: grand unified theories, Technicolor, little Higgs models, and models including extra dimensions [5–8]. The discovery of a new heavy resonance would open a new era in our understanding of elementary particles and their interactions. Other models that contain contact interactions or new particles that mix with the Standard Model particles can lead to modifications of the dilepton spectrum without a resonance are not considered in this report.

The Standard Model of particle physics is a remarkable theory which is able to account for all experimental observations in particle physics. However, there are fundamentally unresolved problems in the Standard Model. The mechanism for electroweak symmetry breaking has not been observed nor has the physical Higgs boson that it predicts. If the Standard Model is valid to the Planck scale, radiative corrections force the parameters of the model to be incredibly finely tuned. Further, although the Standard Model can accommodate many of the observed patterns in nature - it lacks a fundamental explanation for them. Why are there three generations? Why are the quantum numbers of the observed particles - which are crucial for the self-consistency of the Standard Model - what they are? For these reasons, the search for physics beyond the Standard Model is a principle part of the ATLAS physics program.

The strictest direct limits on the existence of heavy neutral particles are from direct searches at the Tevatron [9, 10]. Indirect limits from precision electroweak observables have also been made at the Large Electron-Positron Collider (LEP). The limits are model dependent - but the direct limits are on the order of 600 GeV to 1 TeV while the indirect limits range up to 1.5 TeV [11–15]. The direct searches are ultimately limited by the available center of mass energy and are expected to ultimately be limited to about 1 TeV at the Tevatron [16].

The LHC will have a center of mass energy of 14 TeV, approximately seven times larger than the Tevatron. Ultimately, one expects a corresponding increase in the search reach (5 - 6 TeV). There have been several other ATLAS studies evaluating the potential for discovery of a heavy resonance [17–19]. However, this is the first study to include full trigger simulation, misalignments, and data driven methods. Including these experimental issues is important to realistically estimating the analysis potential.

There are lot of Exotic models which can be tested at the LHC. Analysing all the existing models is impossible due to the limited manpower which is available. Instead we choose to take a different approach, grouping the early-data analyses by their final state topologies. With this approach, we maximise the number of Exotic models that can be investigated. This note covers the dilepton and diphoton final states. We present a template analysis, in which any dilepton or diphoton resonance can be investigated. The strategy followed in this analysis is to understand the Standard Model and the experimental environment first and search for new physics afterwards. In case of discovery, identifying the underlying Exotic model is the natural next step. This subsequent investigation is beyond the scope of this note. We limit ourselves to the 'early data phase' of the experiment, defined roughly to include the accumulation of up to 10 fb^{-1} of ATLAS data. Since this note is primarily concerned with early data, we focus mostly on a detailed understanding of the Standard Model predictions and uncertainties, detector performances, data driven methods, and projections for early running.

We start this note by describing the Monte Carlo Samples in section 2. In sections 3 and 4, we investigate the detector performances concerning the electron, muon, tau and photon reconstruction abilities at high energies and the corresponding trigger efficiencies. In section 5 we investigate the Standard Model limits and the systematic uncertainties which will be used in searching the new resonances in section 6.

2 Monte Carlo Samples

In this section we list the Monte Carlo samples that were used for the studies described in the note. For a detailed description of the generators, procedures, and settings please see [20]. Here we limit the discussion to describing the samples that were used along with the most important parameters. The ATLAS software used throughout the analyses presented in this note is ATHENA release 12 [21]. This release was validated for all aspects of generation, simulation, reconstruction and triggering.

Several heavy resonance samples were used for this study. They are listed in table 1. All signal samples were generated using the PYTHIA [22] event generator program. A detailed choice of parameters is detailed in [20]. The mass of the resonances and the quantity of generated data were chosen by two guidelines:

- Current and expected experimental limits before LHC turn on.
- The accessible mass range assuming less than 10 fb^{-1} of integrated luminosity.

<i>Sample</i>	Dataset	$\sigma \times \text{BR}$	Requirements
Dielectron Samples			
Graviton 500 GeV	5622	187.0 fb	
$Z \prime$ (SSM) 1.0 TeV	5623	506.7 fb	$M_{ee} > 500\text{GeV}$
$Z \prime$ ($E_6 \chi$) 1.0 TeV	5624	380.6 fb	$M_{ee} > 500\text{GeV}$
Graviton 1.0 TeV	5625	6.424 fb	
Dimuon Samples			
Technicolor ρ_T/ω_T , 400 GeV	5620	149 fb	$390.0 \text{ GeV} < M_{\mu\mu} < 410.0 \text{ GeV}$
Technicolor ρ_T/ω_T , 600 GeV	5621	45 fb	$590.0 \text{ GeV} < M_{\mu\mu} < 610.0 \text{ GeV}$
Technicolor ρ_T/ω_T , 800 GeV	5622	17 fb	$790.0 \text{ GeV} < M_{\mu\mu} < 810.0 \text{ GeV}$
Technicolor ρ_T/ω_T , 1.0 TeV	5623	7.5 fb	$990.0 \text{ GeV} < M_{\mu\mu} < 1100.0 \text{ GeV}$
$Z \prime$ (SSM) 1.0 TeV	5601	508.6 fb	$M_{\mu\mu} > 500\text{GeV}$
$Z \prime$ ($E_6 \chi$) 1.0 TeV	5602	380.6 fb	$M_{\mu\mu} > 500\text{GeV}$
$Z \prime$ (SSM) 2.0 TeV	5603	23.8 fb	$M_{\mu\mu} > 1.0\text{TeV}$
Diphoton Samples			
Graviton 500 GeV	5626	377.6 fb	
Graviton 1.0 TeV	5657	12.9 fb	
DiTau Samples			
Graviton 500 GeV	5658	187.0 fb	

Table 1: Monte Carlo signal samples with dataset number, cross section, and generator level requirements.

Unlike the signal samples that were all generated using PYTHIA, the background processes that were considered were generated using several different event generators. The largest physics background to the dilepton channel is expected to be Drell-Yan dilepton production followed by diboson and heavy quark production. In the case of diphotons the largest expected physics is expected to be double direct photon production. Instrumental fakes to both channels are expected to be dominated by dijet and jet + photon production. Table 2 lists the different background samples used in this note.

<i>Sample</i>	Dataset	$\sigma \times \text{BR}$	Generator	Requirements
$Z \rightarrow \mu\mu$	5145	1497 pb	PYTHIA	2μ with $p_T > 5\text{GeV}$
$Z \rightarrow ee$	5144	1497 pb	PYTHIA	$2 e$ with $p_T > 5\text{GeV}$
$Z \rightarrow \tau\tau$	5146	1497 pb	PYTHIA	2τ with $p_T > 5\text{GeV}$
Dijet J0	5009	1.76×10^{10} pb	PYTHIA	$\hat{P}_T = 8-17$ GeV
Dijet J1	5010	1.38×10^9 pb	PYTHIA	$\hat{P}_T = 17-35$ GeV
Dijet J2	5011	9.33×10^7 pb	PYTHIA	$\hat{P}_T = 35-70$ GeV
Dijet J3	5012	5.88×10^6 pb	PYTHIA	$\hat{P}_T = 70-140$ GeV
Dijet J4	5013	3.08×10^5 pb	PYTHIA	$\hat{P}_T = 140-280$ GeV
Dijet J5	5014	1.25×10^4 pb	PYTHIA	$\hat{P}_T = 280-560$ GeV
Dijet J6	5015	360 pb	PYTHIA	$\hat{P}_T = 560-1120$ GeV
Dijet J7	5016	5.71 pb	PYTHIA	$\hat{P}_T = 1120-2240$ GeV
Dijet J8	5017	0.24 pb	PYTHIA	$\hat{P}_T > 2240\text{GeV}$
Drell-Yan ee	5114	200 pb	JIMMY + HERWIG	$M_{ee} > 150$ GeV
Drell-Yan $\mu\mu$	5115	200 pb	JIMMY + HERWIG	$M_{\mu\mu} > 150$ GeV
Drell-Yan $\tau\tau$	5116	200 pb	JIMMY + HERWIG	$M_{\tau\tau} > 150$ GeV
Drell-Yan ee	5614	349.4 fb	JIMMY + HERWIG	$300 > M_{ee} > 450$ GeV, $2 e \eta < 2.8 p_T > 5\text{GeV}$
Drell-Yan ee	5615	89.4 fb	JIMMY + HERWIG	$450 > M_{ee} > 650$ GeV, $2 e \eta < 2.8 p_T > 5\text{GeV}$
Drell-Yan ee	5616	17.7 fb	JIMMY + HERWIG	$650 M_{ee} > 800$ GeV, $2 e \eta < 2.8 p_T > 5\text{GeV}$
Drell-Yan ee	5617	13.5 fb	JIMMY + HERWIG	$M_{ee} > 800$ GeV, $2 e \eta < 2.8 p_T > 5\text{GeV}$
Drell-Yan $\mu\mu$	5624	349.4 fb	JIMMY + HERWIG	$300 > M_{\mu\mu} > 450$ GeV, $2 e \eta < 2.8 p_T > 5\text{GeV}$
Drell-Yan $\mu\mu$	5625	89.4 fb	JIMMY + HERWIG	$450 > M_{\mu\mu} > 650$ GeV, $2 e \eta < 2.8 p_T > 5\text{GeV}$
Drell-Yan $\mu\mu$	5626	17.7 fb	JIMMY + HERWIG	$650 M_{\mu\mu} > 800$ GeV, $2 e \eta < 2.8 p_T > 5\text{GeV}$
Drell-Yan $\mu\mu$	5627	13.5 fb	JIMMY + HERWIG	$M_{\mu\mu} > 800$ GeV, $2 e \eta < 2.8 p_T > 5\text{GeV}$
Drell-Yan $\tau\tau$	5634	349.4 fb	JIMMY + HERWIG	$300 > M_{\tau\tau} > 450$ GeV, $2 e \eta < 2.8 p_T > 5\text{GeV}$
Drell-Yan $\tau\tau$	5635	89.4 pb	JIMMY + HERWIG	$450 > M_{\tau\tau} > 650$ GeV, $2 e \eta < 2.8 p_T > 5\text{GeV}$
Drell-Yan $\tau\tau$	5636	17.7 pb	JIMMY + HERWIG	$650 M_{\tau\tau} > 800$ GeV, $2 e \eta < 2.8 p_T > 5\text{GeV}$
Drell-Yan $\tau\tau$	5637	13.5 pb	JIMMY + HERWIG	$M_{\tau\tau} > 800$ GeV, $2 e \eta < 2.8 p_T > 5\text{GeV}$
$t\bar{t}$	5200	461 pb	MCNLO + HERWIG	At least one leptonically decaying W
WW	5985	24.5 pb	HERWIG	At least one lepton $\eta < 2.8, p_T > 10$ GeV
WZ	5987	7.8 pb	HERWIG	At least one lepton $\eta < 2.8, p_T > 10$ GeV
ZZ	5986	2.1 pb	HERWIG	At least one lepton $\eta < 2.8, p_T > 10$ GeV

Table 2: Monte Carlo background samples including generator, cross section, and generator level requirements .

3 Object Identification and Performance

The high mass dilepton and diphoton final states are promising because of the simplicity and robustness of high p_T leptons and photons reconstruction and identification. None the less, these final states also present unique challenges. For example, how does one establish the reconstruction efficiency, resolution, and linearity of the highest energy leptons from the data itself? How does one optimize the selection criteria? In this section we discuss the performance of the reconstruction and identification of high energy leptons, data driven methods, and studies focusing on topics unique to the highest energy leptons and photons.

3.1 Electrons

The electron identification and performance is described in detail elsewhere [23]; here we concentrate on very high p_T electron reconstruction and identification.

3.1.1 Identification

The background to very high p_T electron pairs is expected to be very low, therefore only minimal selection criteria need to be applied, in order to maximize the efficiency. These minimal criteria are called *loose*. On the other hand, when trying to select very high p_T tau pairs, one cannot demand 2 electrons, and tighter selections are needed.

A cluster reconstructed in the electromagnetic calorimeter is called a *reconstructed* electron if its absolute pseudo-rapidity $|\eta|$ is less than 2.5, and it is associated with a track reconstructed in the tracker within $\Delta R < 0.2^1$.

A first level of *loose* selection can be applied in order to reject highly energetic pions and wide showers. Any associated cluster in the first compartment of the hadronic calorimeter must have an energy which is negligible as compared to the electromagnetic one, and the shower shape and width must be compatible with those of an electron shower in the middle compartment of the electromagnetic calorimeter. The average efficiency of the last two criteria is shown on Figure 1 as a function of generated transverse momentum and pseudo-rapidity for clusters passing the first two criteria and with p_T greater than 50 GeV.

A second level of selection, called *medium*, makes use of the very fine granularity of the first compartment of the calorimeter to reject additional fakes such as single neutral pions. Finally, the impact parameter of the associated track, as measured by the tracker, is required to be compatible with the primary interaction vertex. The average efficiency of these additional selections combined with the two previous criteria is shown on Figure 1 as well for clusters passing the first two criteria and with p_T greater than 50 GeV.

3.1.2 Energy resolution

The calorimeter acceptance can be divided into three parts: the central part of the detector corresponds to $0 < |\eta| < 1.37$, the outer wheel of the end-cap to $1.52 < |\eta| < 2.5$, and the remaining η range ($1.37 < |\eta| < 1.52$) corresponds to the junction (“crack”) between the barrel and the end-cap. In the version of the reconstruction software used in this note, the energy resolution of clusters reconstructed in the electromagnetic calorimeter is slightly above 1% for electrons with an average p_T of 500 GeV, except in the “crack” region where it is about 5%. In this region, there is also a bias on the reconstructed energy

¹⁾The efficiency of the track association is around 15% at low eta in the software release used in this note. It is expected to increase slightly in subsequent versions, see [23].

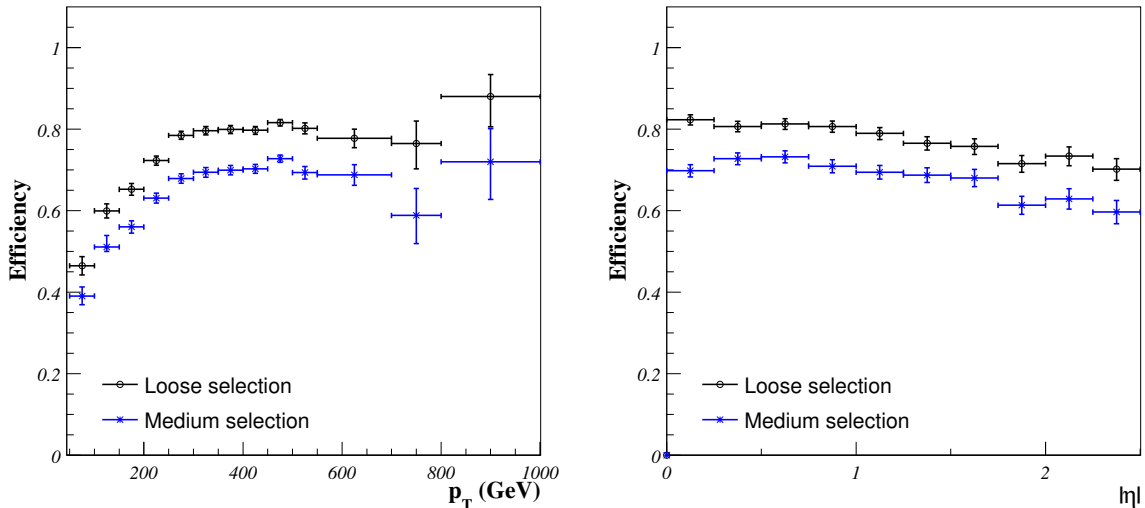


Figure 1: Efficiency of the *loose* and *medium* selection criteria as a function of p_T (left) and η (right).

at the level of a few percent, whereas this bias is negligible in the other parts of the detector (around 0.1%).

3.1.3 Charge reconstruction

As p_T increases, the relative error on its measurement increases. On average, the probability to assign the wrong charge to an electron goes from less than 1 per mil to 5% when the transverse momentum goes from 100 GeV to 1 TeV [24].

3.1.4 Invariant mass reconstruction

The invariant mass of high p_T dielectrons is computed using two ingredients: the energy measurement in the calorimeter, and the direction measurement in the tracker.

One can see on Figure 2 the distribution of the relative difference between reconstructed and generated invariant mass of opposite charge dielectrons with an average invariant mass of 1 TeV. The tail at large $|\Delta M|$ is due to the events in which at least one electron goes into the “crack” region.

A good resolution of $(0.8 \pm 0.02)\%$ and a small non linearity of $(-0.09 \pm 0.02)\%$ are obtained in the Gaussian regime of the distribution.

3.1.5 Bremsstrahlung recovery

High energy electrons can radiate energetic photons. Final state bremsstrahlung recovery of electrons has been investigated. The issue of the study is the correct selection of the photon from the bremsstrahlung among many background photons from jets. A sample of 1 TeV mass Z' decaying to dielectrons pair is used. A dijet sample is also used as a background. We select events which have two opposite charge electrons and a photon, all of them in a pseudo-rapidity range of $|\eta| < 2.5$. The electrons are identified using the *loose* criteria described in section 3.1. Additionally, one requires the electron's $E_T > 20$ GeV and the existence of a photon with $E_T > 15$ GeV.

The photon emitted by electrons coming from a Z' can be selected using the angle between the less energetic electron and the photon in the three-body center of mass system (electron, positron and

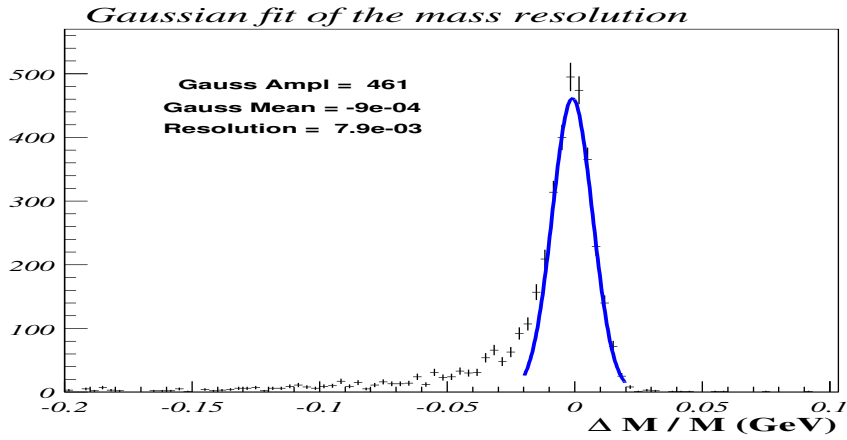


Figure 2: Relative difference between reconstructed and generated dielectron invariant mass.

photon). This angle is expected to be small, as one can see in figure 3. A cut of $\cos(\theta, \gamma)^* > 0.7$ is enough to reject 66% of the background. Only 25% of the events contain a bremsstrahlung photon in the final state and 13% of them pass the cuts above. The dielectron and dielectron-plus-radiated-photon invariant mass distributions for the selected events are plotted in figure 3. This plot shows that the effect of the bremsstrahlung correction is small ($< 1\%$). In the following studies, this correction will not be applied in the dielectron channels.

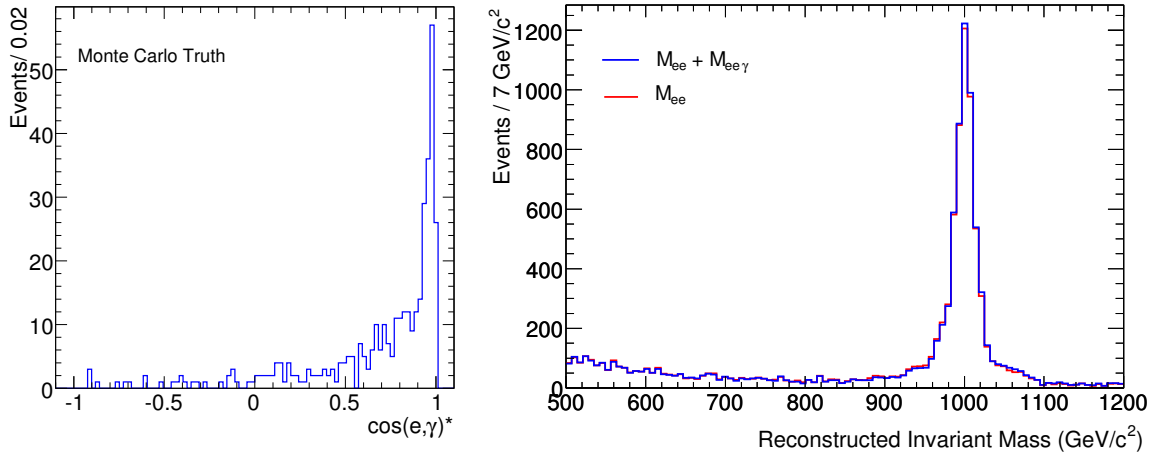


Figure 3: Left: Cosine of the angle between the less energetic electron and the photon. Right: invariant mass distribution for all events with two selected electrons. The blue line represents the events where the radiative correction was taken into account.

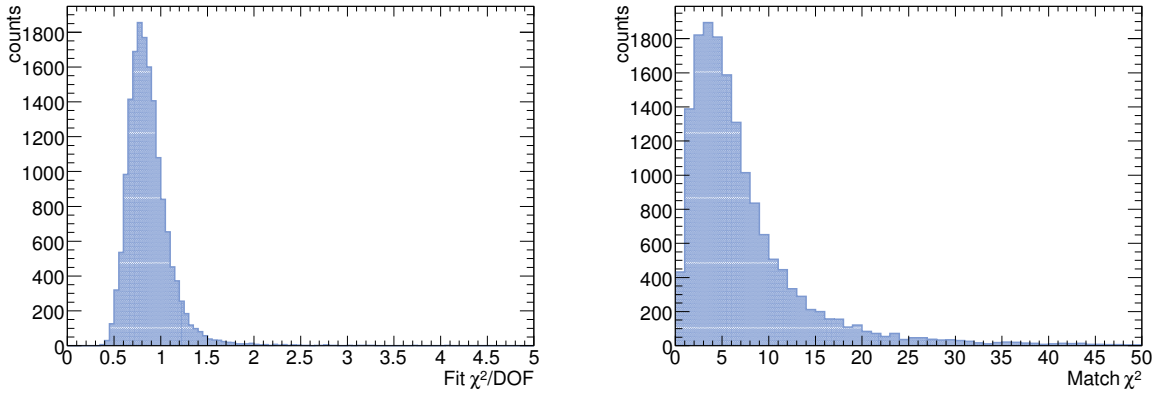


Figure 4: Combined fit χ^2 and match χ^2 for muons with a combined fit in the muon spectrometer and inner detector

3.2 Muon reconstruction and identification

Each of the major subsystems of the ATLAS detector can be used to identify muons. The Inner detector (ID) and Muon Spectrometer (MS) are utilized to find and reconstruct charged particle tracks. The calorimeter can also be used to both identify muons and measure the energy loss the muon suffers while transversing the calorimeter. A full description of the algorithms and muon performance and identification can be found in [25] and [26]. In this section we report on the results of several studies necessary for the dimuon analysis.

3.2.1 Performance on Monte Carlo

In this section we limit ourselves to an evaluation of the performance of the muon reconstruction and identification on the samples of interest. The main backgrounds in the dimuon channel are expected to be real production of high invariant mass muon pairs. Therefore, muon identification requirements are selected in order to maximize the efficiency of dimuon selection only placing very loose requirements to remove very poorly reconstructed muons.

The baseline muon identification (used unless explicitly stated otherwise) requires:

- A combined muon with $|\eta| \leq 2.7$
- Fit $\frac{\chi^2}{DOF} < 10.0$
- Match $\frac{\chi^2}{DOF} < 10.0$
- $p_T > 30$ GeV

Figure 5 shows the efficiency of this event selection on the 1 TeV SSM Z/γ sample as a function of the muon kinematics. The muon reconstruction resolution was also studied and the results shown in figure 6 and figure 7. The results are consistent with previous studies [25] [26]. There are several features in figure 5 that require explanation. In the areas of complete geometric coverage the efficiency of the reconstruction and identification is approximately 95%. At η of 0 there are several services which decrease the acceptance of the spectrometer [25]. In the overlap region between the barrel spectrometer and the end cap (at $1.2 \leq |\eta| \leq 1.4$) there is another geometric loss which explains the dips in efficiency. Finally, the combined reconstruction requires an Inner Detector track which provides coverage up until

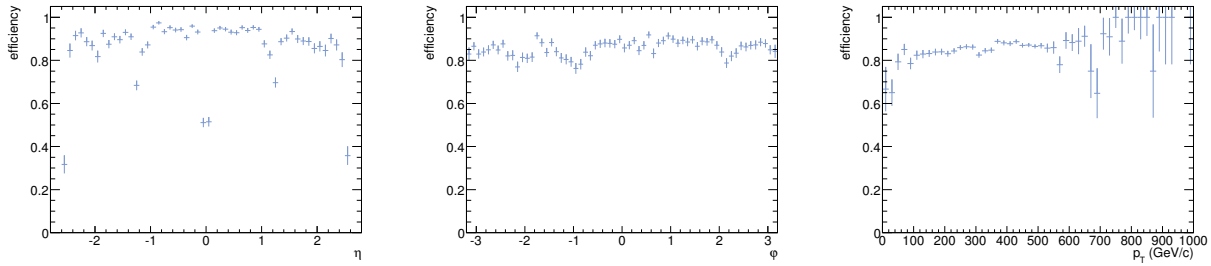


Figure 5: Muon efficiency as a function of η (left), ϕ (center), and p_T (right) evaluated with a 1 TeV Z' sample.

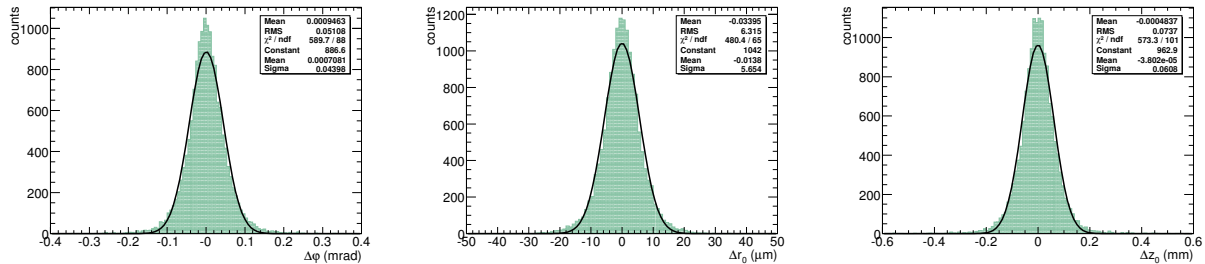


Figure 6: Muon combined track parameter resolution for ϕ (left), r_0 (center), and z_0 (right) evaluated with a 1 TeV Z' sample

η of 2.5. Another feature which can be seen in the efficiency as a function of ϕ is the dips the plot in the center of figure 5. These result from the 'feet' support structure which also reduce the geometric coverage of the spectrometer [25].

3.2.2 Efficiency from data

In the previous section we examined the performance of the reconstruction and muon identification using Monte Carlo truth information. As there may be effects which are not modeled correctly in simulation, it is important to develop a procedure to evaluate the reconstruction efficiency from the data itself. The 'tag and probe' method has been used successfully at the Tevatron. In this method one uses a 'standard candle' as an in situ calibration point. By selecting the $Z \rightarrow \mu\mu$ events and evaluating the reconstruction efficiency from data on these events we show that we can extrapolate into the very high p_T range. A

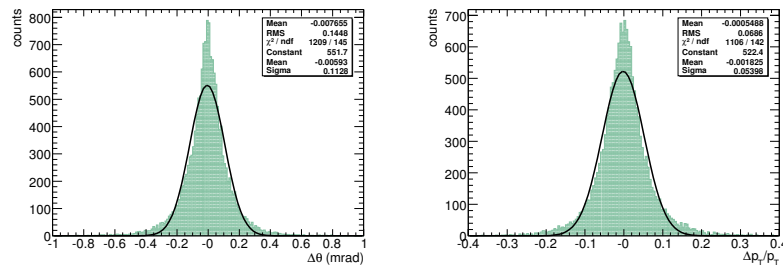


Figure 7: Muon combined track parameter resolution for θ (left) and p_T (right) evaluated with a 1 TeV Z' sample

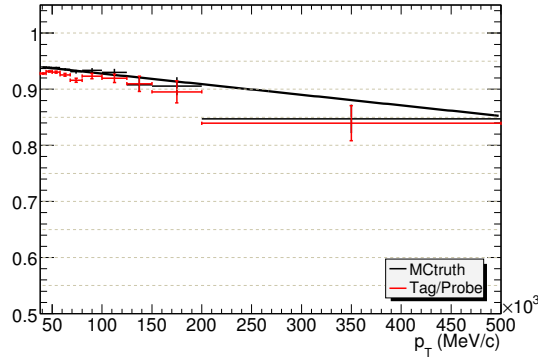


Figure 8: Efficiency as a function of p_T , comparing tag/probe method and Monte Carlo truth.

direct evaluation of the reconstruction efficiency on the highest p_T muons could then be compared with the reconstruction efficiency in high mass dimuon resonance Monte Carlo events.

It is possible to trigger on and select a sample of clean dimuon events without significant background even if the requirements on the selection of one of the muons is loosened. We would like to select events based on evidence that a pair of high p_T muons is produced. A “tag” is defined as a Muon Spectrometer and Inner Detector combined muon track, with a $p_T > 30$ GeV cut. A “probe” is defined as any ID track, also with a $p_T > 30$ GeV cut. All tracks are required to have $\eta < 2.5$ to be within geometrical acceptance. An invariant mass is then calculated from every combinatoric tag/probe pair. Finally, we then select a subsample requiring that the probe muon also be a combined muon track.

The track-finding efficiency of the Muon Spectrometer, ε , is then defined as n/N , where n is the number of dimuon occurrences created from all tag/probe pairs in which the probe ID track was found in the MS, and N is number of pairs in which the identity of the probe ID track remained unknown. Missing MS tracks will result in $n < N$ and thus, efficiency loss.

We have chosen to use a fitting procedure on the Z resonance, which includes a signal and background term. We model the invariant mass distribution of the signal as a combination of two terms:

- A Breit-Wigner resonance convoluted with a Gaussian resolution term to account for the response of the detector.
- An exponential term to account for the γ/Z interference and Drell-Yan production of dimuon pairs off resonance and the combinatoric background of a muon track with a random inner detector track.

In principle, we will also have to account for several small backgrounds (di-jets with decay in flight, heavy quark production, etc.). However, since these are expected to be very small we only note that the method may easily be expanded to allow for other background terms. In this analysis and for the figures below, we have used a sample of approximately 250 thousand events corresponding to ≈ 150 pb $^{-1}$, which is reasonably attainable in the first year or ATLAS running.

The fit function is given by:

$$N \int f(\Gamma, E_0) * g(\sigma) + c_0 e^{c_1 x}, \quad (1)$$

where the convolution integral is normalized and $f(\Gamma, E_0)$ and $g(\sigma)$ are given by

$$\frac{x^2}{(x^2 - E_0^2)^2 + \left(\frac{x^2 \Gamma}{E_0}\right)^2} \quad \text{and} \quad e^{-\frac{1}{2\sigma^2} x^2} \quad (2)$$

respectively. The natural width of the Z resonance, $\Gamma = 2495.2$ MeV, remains fixed. The fit parameters include N (or n), the mean mass value E_0 (≈ 91 GeV/c²), and σ , the width of the Gaussian resolution (≈ 2 GeV/c²).

When finding $\varepsilon(p_T)$, we choose not to use an exponential background term for ID tracks with p_T greater than 30 GeV (fitting without the background term changes the value of N by less than 0.5%). In this simple case, the error on the tag/probe efficiency is determined using a binomial distribution. In the case where the background term is non-zero (especially when QCD background is included), the efficiency error is determined from a propagation of the fit errors associated with n and N (dn and dN, respectively), and is given by

$$d\varepsilon^2 = \left(\varepsilon \frac{dN}{N}\right)^2 + (1 - 2\varepsilon) \left(\frac{dn}{n}\right)^2. \quad (3)$$

This can be shown to reduce to a binomial expression in the non-background limit.

Using this method, we have been able to use the long Z resonance tail to find track-finding efficiencies of the MS out to p_T of ~ 500 GeV/c, which are consistent with Monte Carlo truth. Eventually the tag/probe fits will be used on first-year $Z \rightarrow \mu^+\mu^-$ signal data to anchor efficiency trends.

3.2.3 Extrapolation to high p_T using the tag/probe method

In the tag/probe method, we find a decrease in efficiency as a function of p_T over 500 GeV.

The result of fitting a first order polynomial to the Monte Carlo efficiency distribution as a function of p_T , as shown in figure 8, is

$$(0.9468 \pm 0.0022) - (1.89 \pm 0.41) \times 10^{-7} p_T. \quad (4)$$

Some Monte Carlo studies have been done to compare muon efficiencies as a function of η for $Z \rightarrow \mu^+\mu^-$ and $1 \text{ TeV}/c^2 Z' \rightarrow \mu^+\mu^-$ samples. As seen in Figure 9, most of the efficiency drop appears in the end-cap region. To study this effect further, we have looked at the efficiency versus p_T in two main η regions: $0.2 < |\eta| < 1.0$ and $1.4 < |\eta| < 2.5$, representative of the barrel and end-cap regions, respectively (figure 9). However, the polynomial in equation 4 seems to underestimate the efficiency found in the Z' sample.

The cause of the efficiency loss at very high momentum was determined to be showering from very high muons inside the hadronic calorimeter and in the muon spectrometer itself. When the muon was seen to shower in the muon spectrometer this could occasionally lead to one of two effects. The pattern recognition in the muon spectrometer could fail due to the complexity and extent of the shower. In this case no track was reconstructed in the muon spectrometer. Other tracks were found in the muon spectrometer however one or more hit from a shower particle was associated to the original muon track. In this case the track parameters can be very poorly reconstructed leading to a failure when attempting to combine with an inner detector track. figure 10 shows the efficiency of both standalone and combined muon efficiency as a function of the number of hits in a cone around the Monte Carlo truth muon. As the showering becomes more extensive the efficiency drops off.

3.2.4 Charge Misidentification

We have studied the rates and causes of misidentifying the charge of reconstructed muons. The misidentification is determined by comparing the charge of reconstructed muons to the corresponding Monte Carlo truth muons. We then calculate the mis-identification probability as a function of muon p_T , η , and ϕ .

Single muons with a fixed p_T of 500 GeV were used to study charge misidentification at high momenta. The selection criteria were the following:

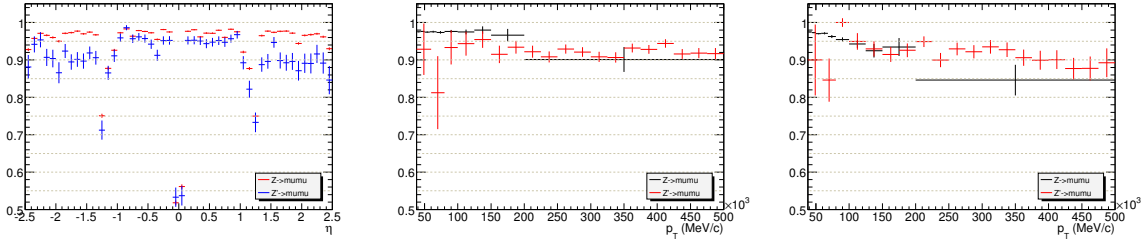


Figure 9: Efficiency as a function of muon Monte Carlo truth η (left) and p_T in the barrel(center) and endcap(right), comparing Z, Z' parents

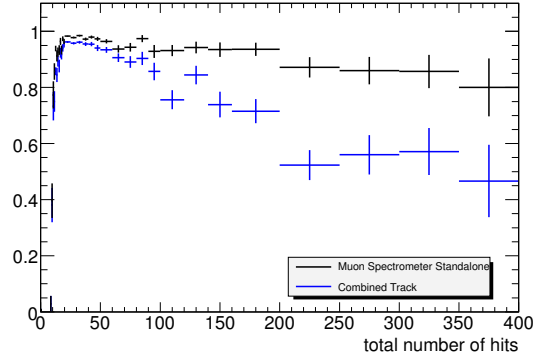


Figure 10: Efficiency of track finding of muon spectrometer standalone and combined tracks as a function of the number of hits in a cone around the Monte Carlo truth muon.

- $p_T > 25 \text{ GeV}$
- Fit $\chi^2/DoF < 10$
- Match $\chi^2/DoF < 10$

Figure 11 shows the mis-identification rate from Muid as a function of p and $|\eta|$ as the selection criteria are applied. Within statistics, the mis-identification rate is flat in ϕ .

3.2.5 Radiative Effects

Muons decaying from heavy new particles, such as Z' or Randall-Sundrum(RS) G^* , are expected to have very high momentum. For muons above few hundred GeV, the radiative process becomes more important than ionization loss. These radiative processes are electromagnetic (e^+e^- pair production, bremsstrahlung) and photo-nuclear interactions in the calorimeter [27].

The calorimeter correction algorithms and their performances for radiative muons have been studied in detail [28]. In the reconstruction, the energy depositions in the electromagnetic and hadronic calorimeters associated to the isolated muons are corrected for. In the ATLAS detector, muons of $1 \text{ TeV}/c$ at $0.4 < |\eta| < 0.5$ are expected to have most probable energy-loss of 5 GeV, and a mean energy-loss of 14 GeV [28], which is not totally negligible.

The effect of radiative muons in the decay of SSM Z' for masses of 1 and 2 TeV/c^2 has been studied. The reconstructed dimuon mass is shown in figure 12. The mass shift due to radiative muons is clearly visible. The relative mass shift due to radiative muons for SSM Z' of $1 \text{ TeV}/c^2$ is shown in figure 13.

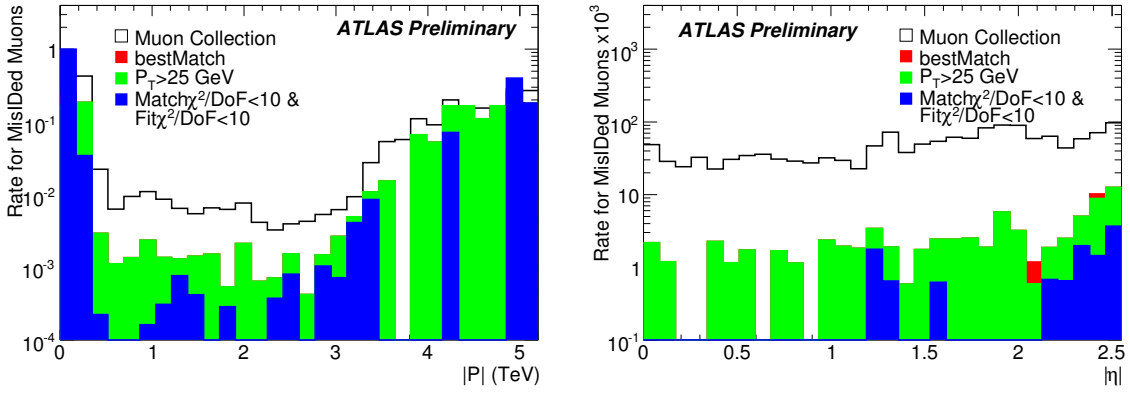


Figure 11: The charge misidentification rate as a function of muon p (left) and $|\eta|$ (right).

While -2.4% mass shift is observed without the calorimeter energy correction, the radiative muon effect can be corrected for with proper treatment of showers in the calorimeter associated to the isolated muons.

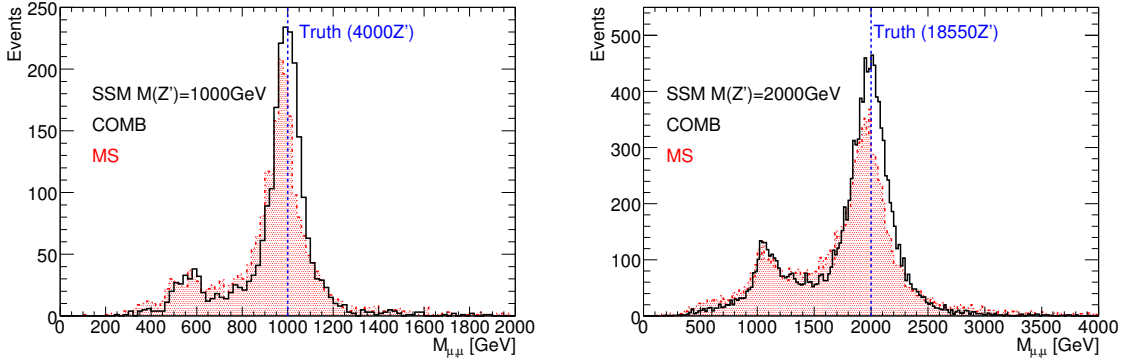


Figure 12: Reconstructed dimuon mass for SSM Z' of $1 \text{ TeV}/c^2$ (left) and $2 \text{ TeV}/c^2$ (right). The hatched histogram shows the reconstruction with muon station only (MS). The open histogram shows the combined reconstruction of muon station and inner detector (COMB) with calorimeter energy corrections.

3.2.6 Effects of Misalignment

In the range of muon energy considered in the analysis, the momentum resolution is dominated by the intrinsic accuracy of the Monitored Drift Tube (MDT) and the chamber alignment. The goal of Muon Spectrometer (MS) alignment system is to reach an accuracy of 40 microns on the alignment contribution to the sagitta measurement. Nevertheless, given the difficulty in controlling the sensors positioning and calibration, it is very unlikely that this figure will be reached at the start of the data taking and one has to consider the case of worse alignment performances for the first year(s) of operation aims at controlling the measured sagitta. In this note, we shall consider several scenarios corresponding to different degrees of the understanding of the alignment system.

The position of each station (MDT+RPC in the barrel part of the spectrometer, MDT and TGC separately in the End cap parts, the CSC not being moved) is described by a set of 6 alignment constants corresponding to the three translations along the (x,y,z) axis of the local coordinate system of the station and to the three rotations around these axis. The zero values correspond to the nominal chamber positions.

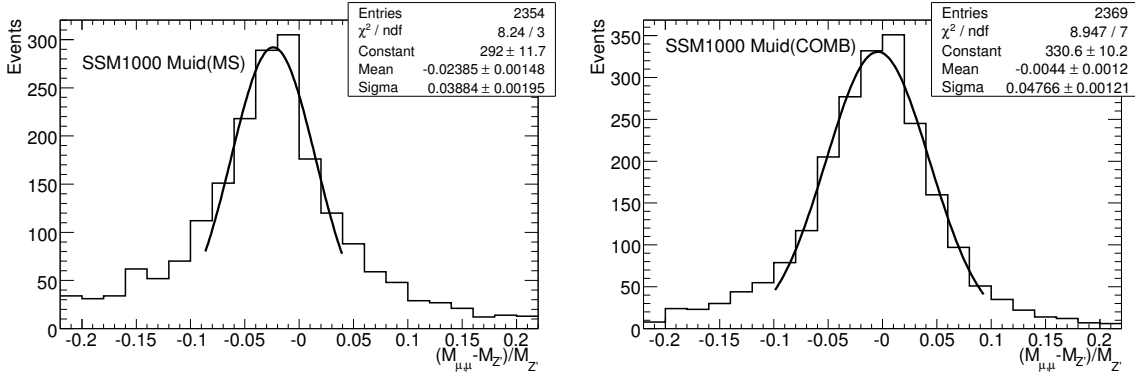


Figure 13: Relative differences between the reconstructed and the generated dimuon masses for SSM Z' of $1 \text{ TeV}/c^2$. The upper histogram shows the reconstruction with muon station only (MS), the lower histogram shows the combined reconstruction of muon station and inner detector (COMB) with calorimeter energy corrections.

For this note, we choose to simulate the chambers misalignment by generating independent random Gaussian translations and rotations of the chambers, hence ignoring correlations that would be expected from a full simulation of the optical system. For each misalignment scenario, we shall assume a set of Gaussian sigmas for the 3 translations and the 3 rotations. For simplicity, we have taken the same sigma for all three translations, ranging from $\sigma_{x,y,z} = 1 \text{ mm}$ for the most pessimistic scenario to $\sigma_{x,y,z} = 40 \mu\text{m}$ for the final performances. We shall also assume that all rotations sigmas are identical and scale with the translation sigma with the correspondence $\sigma_{rot}(\text{mrad}) = 0.5\sigma_{trans}(\text{mm})$. This correspondence is chosen such that the impact from translations and rotations on the chamber corners positions is similar. These values can be compared to the expected initial positioning accuracy of the chambers: $\sigma_{trans} \approx 5$ to 10 mm , $\sigma_{rot} \approx 2$ to 4 mrad .

The impact of the Inner Detector (ID) alignment, together with the relative alignment of the Muon Spectrometer and the ID (not worked out by the time of this note), have not been considered as in this momentum range the ID contribution to the resolution is expected to be marginal. Still, their impact on the combined reconstruction efficiency may not be negligible and will deserve a future dedicated study.

In order to save on simulation time (which is the dominant CPU consuming process), the events (signal and background) are generated with only one initial set of alignment constants. This initial misaligned geometry corresponds to the combination of two movements:

- A global distortion of the barrel.
- A random movement, as described above, with $(\sigma_{trans} = 1 \text{ mm}, \sigma_{rot} = 1 \text{ mrad})$.

The misalignment studies are based on changing the geometry at the reconstruction stage by adding new random displacements on top of the initial geometry which are supposed to account for the wrongly controlled alignment as described in the introduction. We have checked that this procedure is equivalent (within the statistical accuracy) to the inverse strategy which consists in simulate different samples with different geometries and reconstructing them with the same geometry.

For the analysis, we have chosen 7 different hypotheses of misalignment: $(40\mu\text{m}, 20\mu\text{rad})$, corresponding to the target value of the alignment system, $(100 \mu\text{m}, 50 \mu\text{rad})$, $(200 \mu\text{m}, 100 \mu\text{rad})$, $(300 \mu\text{m}, 150 \mu\text{rad})$, $(500 \mu\text{m}, 250 \mu\text{rad})$, $(700 \mu\text{m}, 350 \mu\text{rad})$ and $(1000 \mu\text{m}, 500 \mu\text{rad})$. In the last two cases, the alignment resolution is of the order of or higher than the track sagitta we want to measure.

Table 3: Integrated reconstruction efficiency

Misalignment (μm)	Nominal	40	100	200	300	500	700	1000
Integrated efficiency chi	0.786	0.785	0.786	0.782	0.785	0.786	0.782	0.77
Integrated efficiency SSM	0.793	0.793	0.793	0.793	0.788	0.787	0.783	0.772

For this misalignment analysis, we considered 1 TeV Z' , from two models Chi and SSM. The charge misidentification and misalignment studies are based on these Z' datasets only.

The reconstruction event selection is based on the following requirements and cuts:

- At least two Muon Spectrometer muons with $p_T > 20$ GeV for the signal and the high-mass Drell-Yan,
- The two tracks with the highest momenta have opposite charge
- $|\eta| < 2.7$

The number of selected events for the two Z' datasets are respectively 43 for the chi and 54 for the SSM corresponding for an integrated luminosity of 100 pb^{-1} .

For the efficiency studies, the association of reconstructed with generated muons is based on the following criteria. For each simulated track, we look for reconstructed tracks inside a cone of normalized width n , $|(X_{rec} - X_{sim})| \sigma_{X_{rec}} < n$ with $X = \theta$ or ϕ and such that $|(1/P_{rec} - 1/P_{sim})| \sigma_{1/P_{rec}} < m$. If several reconstructed tracks are associated with a given simulated one, the nearest one in terms of angular distance is taken as match. The default values (derived from single muon events studies) are $n = m = 100$. All the reconstructed tracks that could not be associated by this procedure are considered as fakes.

The pattern recognition efficiency is only mildly affected by the chamber alignment, see table 3. As shown in the next section, the main impact on event selection efficiency will come from the charge misidentification.

The figure 3.2.6 shows the resolution $\frac{\Delta(\frac{Q}{p})}{\frac{Q}{p_{Gen}}}$ of the muon spectrometer as a function of the misalignment hypothesis.

For large misalignments and large p_T , the values of the resolution shows that a significant fraction of the muons will have a wrongly reconstructed charge. The MS measures the track sagitta in the (r,z) bending plane, where r is the radial axis in the mid-plane of a sector and z the standard ATLAS longitudinal axis. This sagitta is built out of the z measurements in the three inner, middle and outer stations and is an algebraic quantity, the sign of which is related to the particle charge. An example of charge misidentification rate for 500 GeV muon at low η is shown on figure 15, assuming a random 1mm misalignment on the sagitta. As the sagitta for this momentum value is also 1mm, the charge misidentification is expected to be 16%.

Figure 16 shows the charge identification efficiency as a function of p_T for the different levels of misalignment. The results in Figure 16 are consistent with the estimation of the number of charge misidentified muons for the 1mm misalignment. For the plot on the bottom right, the fact that the charge misidentification is very low is due to the CSC chambers which are not moved in the layout.

For a 1 TeV Z' , table 4 gives the loss in signal efficiency due to the charge misidentification when the event selection requires two opposite sign muons.

Table 4: loss in signal efficiency due to the charge misidentification for different misalignment hypotheses

Misalignment (μm)	Nominal	40	100	200	300	500	700	1000
Relative loss	0.984	0.984	0.984	0.98	0.973	0.948	0.918	0.877

3.2.7 Z' invariant mass for different misalignment hypotheses

As shown in Figure 17 (left), the dominant effects leading to a wash out of the signal are the resolution loss and the increase of charge misidentification rate as the misalignment is increasing.

For assessing the impact of the alignment on the background level under the Z' signal, we shall consider only the dominant background Drell-Yan. The DY events samples have been reconstructed for different misalignment scenarios. The results are shown in Figure 17 (right). The background level increase is significant for the large misalignment levels. The loss of significance due to the wash out of the signal peak and the increase of background levels at high $M_{\mu\mu}$ mass is summarized in table 4. The mass window is defined from a fit to the mass distributions assuming that $1/M$ distributions are Gaussian, the width being equal to 2 standard deviations.

Resolution vs Pt

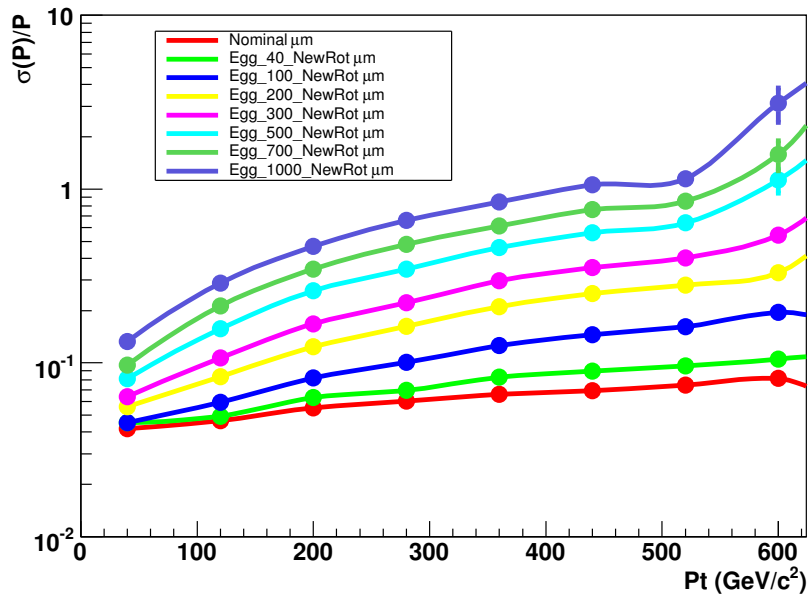


Figure 14: Momentum resolution versus p_T .

sagitta distribution

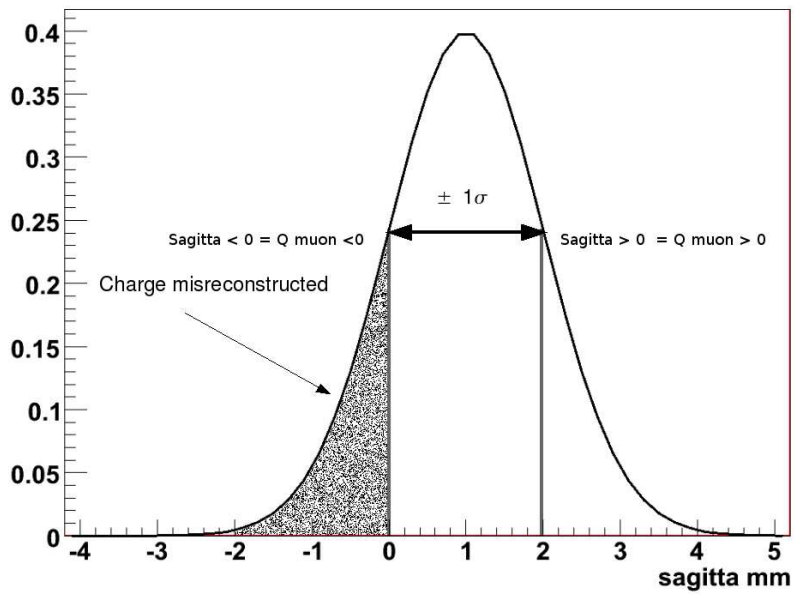


Figure 15: Sagitta distribution for 500 GeV muons and 1 mm alignment resolution.

3.3 Photons

The identification of photons has largely been devised in studies for $H \rightarrow \gamma\gamma$ and its backgrounds. The typical momenta of these photons is far below that for photons from a typical heavy exotic resonance. In the case of the graviton, the difference of regime is so large that potentially different performance might hold. For instance, as energies increase the depth of photon showers in the calorimeter will increase. In addition, noise and other energy deposits near isolated photons may look different for photons at 100s of GeV. These p_T -dependent effects can complicate a graviton search because they modify the shape of background yields vs. $M_{\gamma\gamma}$. Simulated samples will require separate p_T -dependent corrections to their cross sections motivated from theoretical concerns. A more constant photon performance will simplify their determination.

We have studied high p_T photon performance to support a high mass $G \rightarrow \gamma\gamma$ search. In this section, we discuss a determination of the photon efficiency vs. p_T and η . An observed inefficiency from the isolation requirement is addressed by a modified selection tuned to provide constant efficiency as a function of p_T . We also provide an estimate of the photon fake rate at high p_T from multiple samples.

3.3.1 Acceptance and Efficiency Determination

The photon efficiency for the Graviton sample is calculated using the baseline photon ID cuts and applying no isolation cut. The reason for this is that a flat cut on isolation energy causes the efficiency at higher p_T to decline. We determine a more optimal isolation selection in the next section. The efficiency for photons is calculated by matching truth photons from the Graviton to reconstructed photons within $\Delta R (= \sqrt{\Delta\eta^2 + \Delta\phi^2}) < 0.1$. We use the Graviton samples in order to reach the energy range needed, as well as to determine the efficiency in a physics event as opposed to a one-particle event. Figures 18 to 21 show the efficiency of the photons in the Graviton sample vs p_T and η respectively. Efficiencies for photons in both the 500 GeV and 1 TeV Graviton samples are shown.

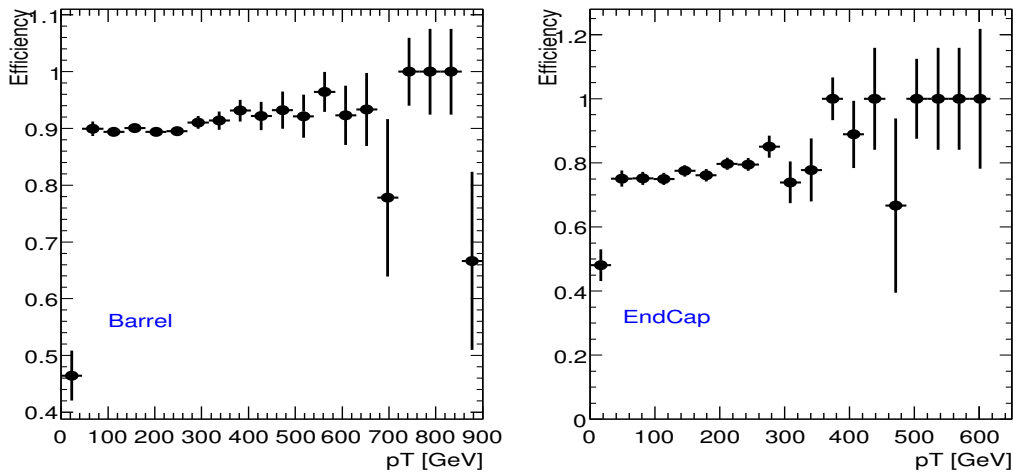


Figure 18: Photon efficiency in 500 GeV Graviton sample vs p_T , with no isolation cut. Barrel (left) and Endcap (right) performance is shown.

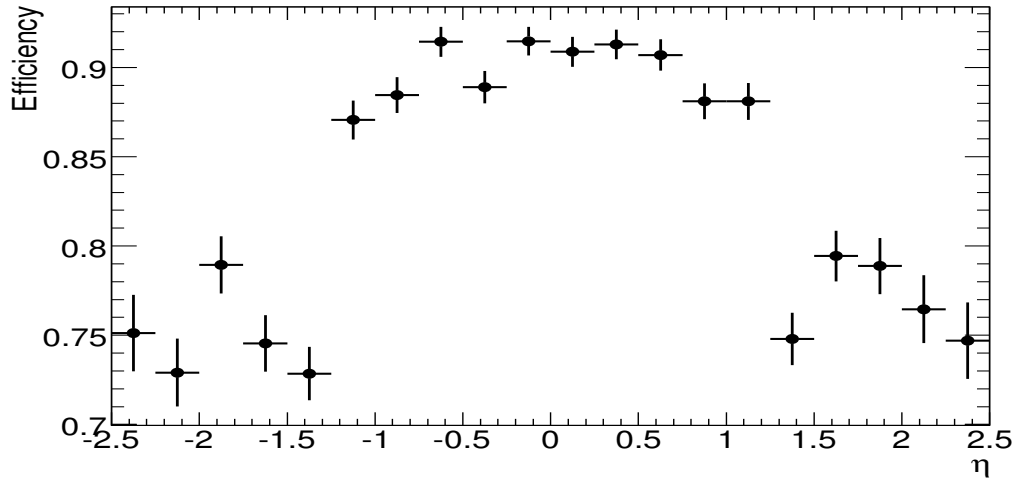


Figure 19: Photon efficiency in 500 GeV Graviton sample vs. η , with no isolation cut.

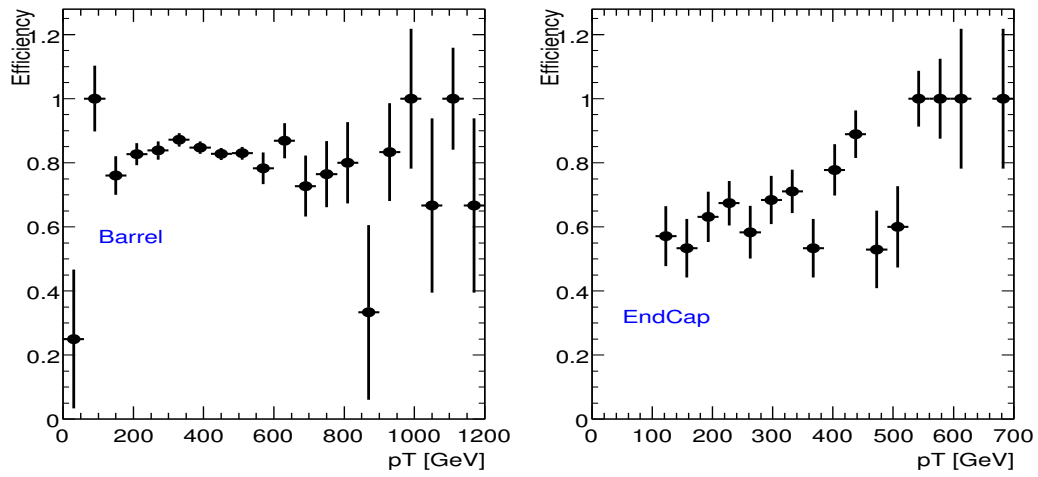


Figure 20: Photon efficiency in 1 TeV Graviton sample vs. p_T , with no isolation cut. Barrel (left) and Endcap (right) efficiencies are illustrated.

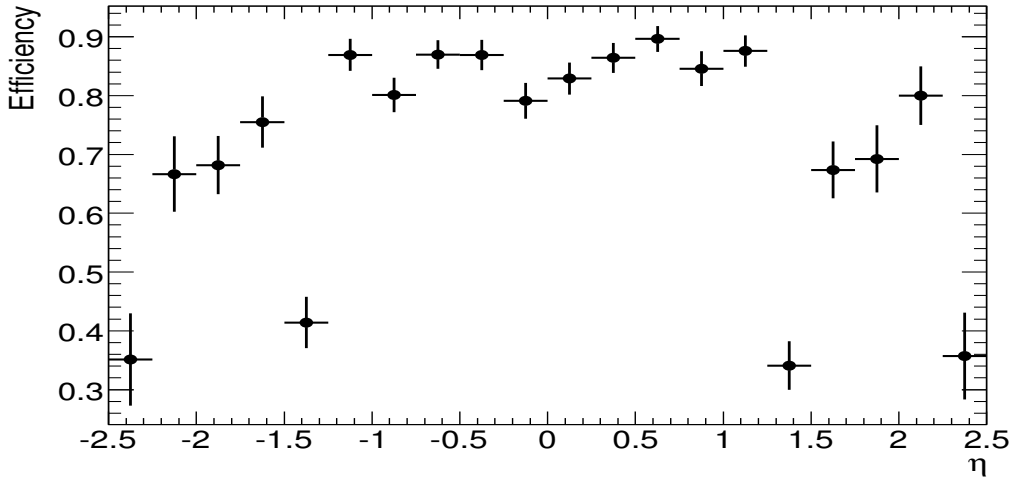


Figure 21: Photon efficiency in 1 TeV Graviton sample vs. η , with no isolation cut.

3.3.2 Isolation Optimization

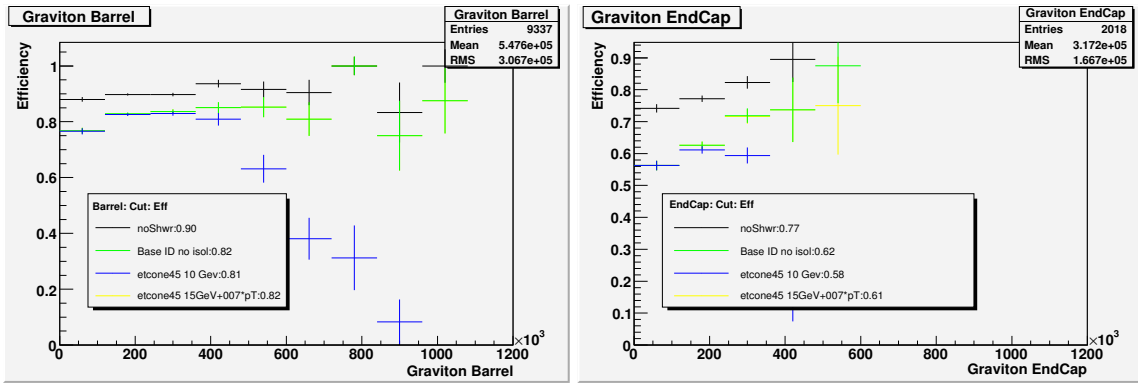


Figure 22: Photon efficiency in 500 GeV Graviton sample vs. p_T for Barrel (left) and Endcap (right).

Isolation selections involving the calorimeter energy in a cone of size 0.45 (i.e. *etcone45*) from a photon centroid were studied. As shown in figure 22, the efficiency vs. photon p_T declines rapidly above 400 GeV when the isolation condition on the *etcone45* variable is included. The isolation energy cut must be optimized for signal and background samples. Figures 23 and 24 show the *etcone45* value for the various signal and background samples. From these plots we see that it's possible to remove some of the events from the dijet sample since they seem to be systematically above the value for the Graviton sample. Since the dijet J5 sample has the largest cross section, 12500 pb^{-1} , by several orders of magnitude of all the other background samples it is promising that this cut can potentially reduce this background significantly.

The QCD cross sections are such that a search without an isolation cut is untenable. To optimize a variable which would produce more constant efficiency with p_T , we employed the Toolkit for Multivariate Analysis (TMVA) to design cuts in photon p_T bins. A linearly p_T -dependent selection was determined for barrel and endcap photons which is indicated in the legend for figure 22. The yellow

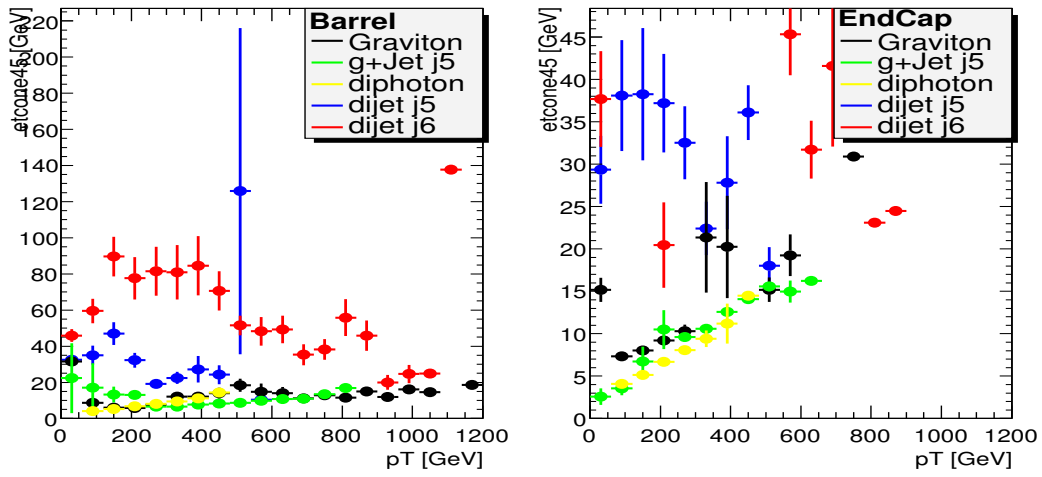


Figure 23: Profile plot of isolation cone 45 variable for all samples.

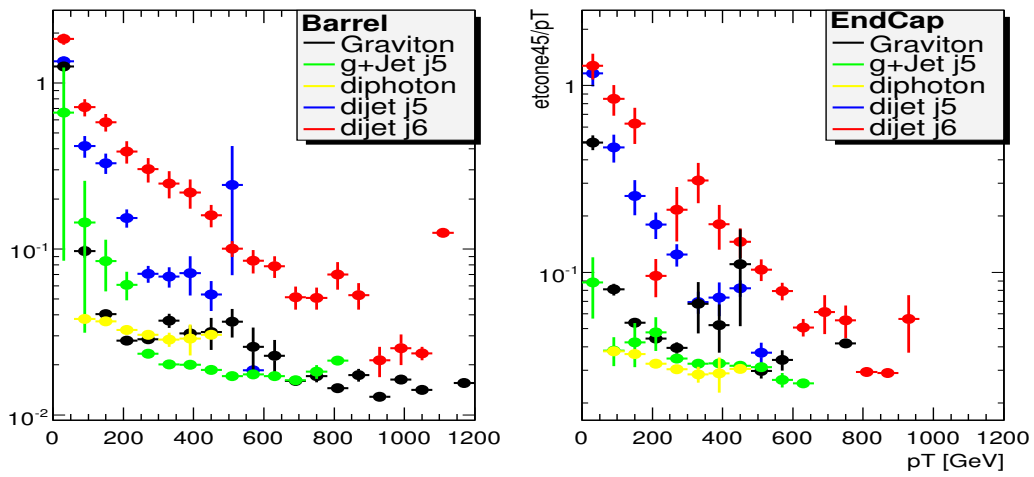


Figure 24: Profile plot of relative isolation cone 45 ($\frac{etcone45}{p_T}$) variable for all samples.

points generally lie under the green ones, indicating a very efficient and p_T -independent isolation efficiency in both the barrel and endcap.

3.3.3 Fake Rate Estimation

Jets, through their fragmentation to leading π^0 s mainly, may manifest as highly electromagnetic, isolated clusters of energy which can pass typical photon identification selection. The rate at which jets fake photons may not be well reproduced in the Monte Carlo because it is sensitive to the specifics of jet fragmentation, and of particle showering in the calorimeter, which are challenging particularly in a crowded environment. Nevertheless, we may be able to extract order-of-magnitude estimates of these rates from the simulation. More importantly, by extracting and studying these rates, we can investigate the feasibility of our method of estimating instrumental backgrounds from data.

To estimate the fake rate, we counted the number of true Jets in the Dijet J5 and J6 samples. We remove the reconstructed photons which have a matching true photon. The ratio of the number of photons as a function of p_T and the number of true jets as a function of p_T gives the number of fake photons which come from jets. Figure 25 shows the fake rate for the dijet samples.

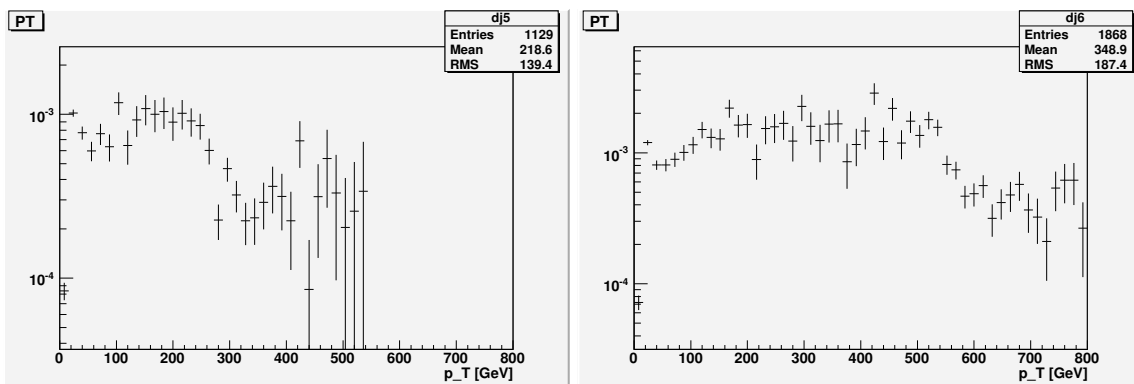


Figure 25: Photon fake rate for Dijet J5 (left) and J6 (right) samples.

We have also calculated directly the jet-to-photon fake rate according to the prescription of the EGamma group. A jet is said to be misidentified as a photon when a truth jet is within $\Delta R < 0.2$ of a reconstructed photon. Table 5 provides the measured fake rates in the barrel and endcap using the two dijet samples. We also provide the rate to be reconstructed as an EGamma, vs. the rate to be fully identified as a photon, in the J5 sample.

Table 5: Photon fake rates for J5 and J6 samples.

Sample	isEM cut	Barrel	Endcap	total
J5	no cut	0.073	0.043	0.054
J5	= 0	0.0035	0.0	0.0019
J6	= 0	0.0081	0.0007	0.0050

3.4 Tau Identification

In this section we focus on optimizing the rejection of jets coming from QCD di-jet production while still providing an efficient identification of high P_T taus. The transverse momentum range of the taus coming from Z' boson extends up to 600 GeV with a sharp peak at 300 GeV and an average P_T of the visible decay products at 140 GeV.

The reconstruction of hadronic τ -candidates was done using the generic package tauRec [29]. The algorithm is calorimeter based, starts from a reconstructed cluster with $E_T > 15$ GeV and then builds identification variables based on information both from the Electromagnetic Calorimeter (ECAL) and the Hadronic Calorimeter (HCAL) as well as from the Inner Detector (ID). A cluster is called a reconstructed τ if a true τ -jet was found in a cone of $\Delta R < 0.3$ ¹⁾. The package does not provide any discrimination against electrons or muons either at reconstruction or at identification level, therefore a significant fraction of true electrons and some muons (87.6% and 4.8 % respectively) are reconstructed as hadronic taus. In order to avoid "double-counting", a reconstructed tau matching an isolated and identified lepton (an electron or a muon) in a cone of $\Delta R < 0.2$ around the τ -jet axis is not considered as a hadronic tau.

Figure 26 shows the reconstruction efficiency, which is defined as the probability of a true hadronic tau to be reconstructed as a cluster, as a function of E_T ²⁾, η and ϕ . In the plots showing the tau identification efficiency as a function of E_T and ϕ only true hadronic taus within $|\eta| \leq 2.5$ were considered. The efficiency for the e/μ - τ -jet overlap removal, defined wrt all reconstructed taus is also plotted in figure 26

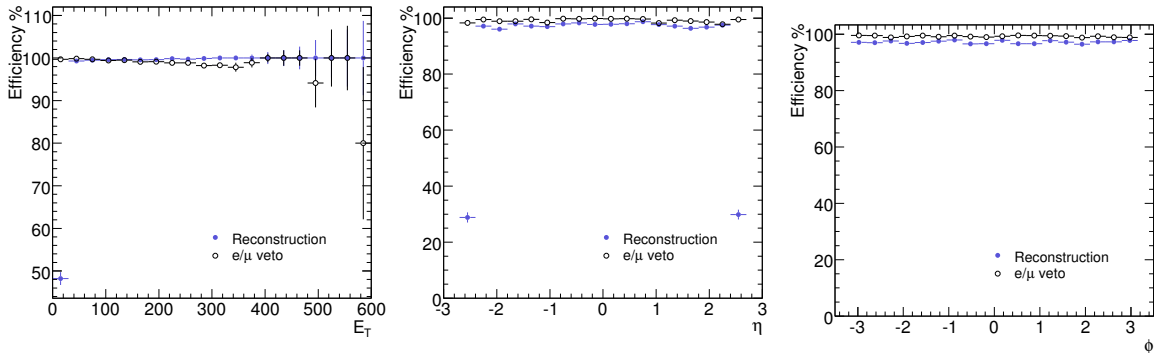


Figure 26: Reconstruction efficiency and overlap removal efficiency as a function of E_T , η and ϕ .

The efficiencies are summarized in table 6. The reconstruction efficiency is normalized to all true hadronic taus with $E_T > 15$ GeV inside the η acceptance. Efficiencies for electron and muon veto are given wrt all reconstructed taus. The electron and muon misidentification rates are normalized to true electrons or muons inside of the acceptance ($|\eta| < 2.5$ and $E_T > 15$), respectively.

Tau jets are well-collimated low track multiplicity jets with hadronic and electromagnetic energy depositions. Several variables have been considered in the tauRec package to exploit these properties³⁾. They are combined into one discriminant based on a likelihood method which was proven to give the best tau identification and QCD jet-rejection [29]. At high E_T the number of associated tracks provides the best discrimination against background since the QCD jets become very collimated at high E_T and tend to form narrower showers.

¹⁾ $\Delta R = \sqrt{\Delta\eta^2 + \Delta\phi^2}$

²⁾if not stated differently E_T denotes E_T of the visible decay products

³⁾Complete list of variables can be found in [29].

Events in $\eta \leq 2.5$ (MC truth)	$87.1 \pm 0.1 \%$
Events in $\eta \leq 2.5$ && $E_T > 15$ GeV (MC truth)	$85.6 \pm 0.2 \%$
Reconstruction	$98.8 \pm 0.1 \%$
Electron veto	$99.3 \pm 0.1 \%$
Muon veto	$99.9 \pm 0.0 \%$
Electron - τ^{had} misidentification	$46.4 \pm 0.6 \%$
Muon - τ^{had} misidentification	$3.8 \pm 0.3 \%$

Table 6: Reconstruction efficiency, efficiency of e/μ - τ -jet overlap removal and electron/muon misidentification for τ 's from Z' . For completeness, the efficiencies for kinematic cuts are also given.

Figure 27 summarizes the performance of this approach in four different E_T bins. On the right plot the efficiency for τ 's from Z' as a function of likelihood cut is shown. The left plot shows the cross section weighted number of fake taus from QCD jets for 1 fb^{-1} of data as a function of the highest likelihood jet in the event. Despite the fact that the likelihood was tuned in 11 E_T bins, it shows a strong E_T dependence. A fixed cut on likelihood will not result in flat efficiency, nor will it be optimal for jet rejection. Hence an E_T dependent cut should be applied as also argued in [29].

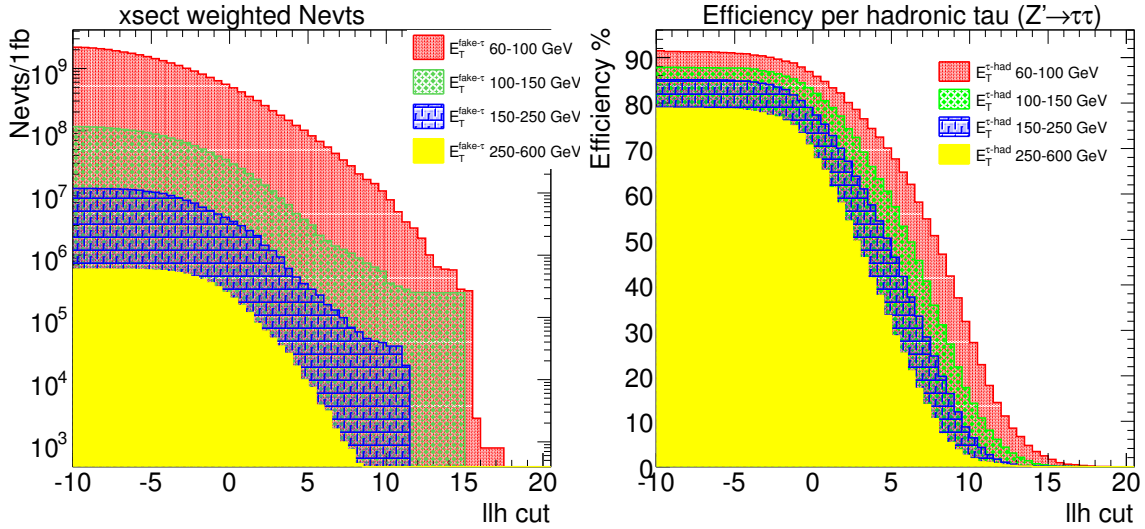


Figure 27: Left: Cross section weighted number of events per 1 fb^{-1} of data as a function of llh cut for four different E_T bins. The highest llh fake tau is selected first for every event. QCD di-jet samples with a hard process p_T of 35-1120 GeV were used. Right: Efficiency as a function of the llh cut given per hadronic tau from Z' for four different E_T bins.

To discriminate against background the hadronic tau is required to have $E_T > 60$ GeV, from 1 to 3 tracks, and fulfill an E_T dependent llh cut (6, 4, 2, 0 for E_T ranges 60-100, 100-150, 150-250, >250 GeV, respectively). The efficiency of such pre-selection and identification as a function of E_T , η and ϕ is shown in Figure 28. and the exact values are summarized in table 7. The clear drop in efficiency starts around $|\eta| = 1.3$ when requiring $1 \leq N_{\text{trk}} \leq 3$. This reflects the non-uniform geometry of the ID: i) crack region in the Silicon Detector at $|\eta|=1.3$ ii) crack region in the Pixel Detector at $|\eta|=1.7$ and iii) absence of TRT tracking in a region $2.0 < |\eta| < 2.5$. The additional drop in efficiency after applying cuts on the likelihood is observed around $|\eta|=1.5$. This corresponds to the crack regions in ECAL which affect calorimeter based identification variables.

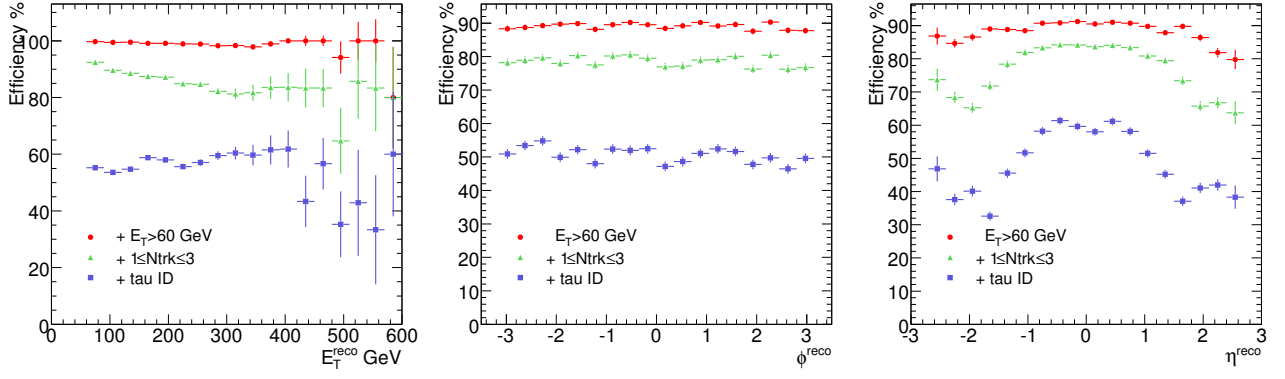


Figure 28: Efficiency wrt to all reconstructed taus after removal of the overlap with e or μ as a function of E_T , η and ϕ .

Cut	Efficiency %
$E_T > 60 \text{ GeV}$	89.8 ± 0.2
$+1 \leq N_{\text{trk}} \leq 3$	79.2 ± 0.3
+lh cut	51.0 ± 0.3

Table 7: Preselection and identification efficiency for $Z' \rightarrow \tau\tau$. Efficiency is given wrt reconstructed hadronic taus (after removal of overlap with e or μ).

For the reconstruction of the tau energy, all cells within $\Delta R < 0.4$ around the barycenter are used. Cells are calibrated with an H1-style calibration [30], with cell weights optimized for jet calibration. This method overestimates the energy of the tau by 3-4 %, excluding the crack regions in EMCAL ($|\eta| \sim 1.5$) where tau energy is underestimated. The relative energy resolution (mean divided by σ) of the taus after preselection and identification is 6.5% and improves at higher energies when taus become more collimated.

4 Trigger Requirements

4.1 Introduction

At a nominal luminosity of $\mathcal{L} = 10^{34} \text{ cm}^{-2}\text{s}^{-1}$ the interaction rate seen in the ATLAS detector will be around 1 GHz [31], which is far too high to be written to mass storage. The aim of the trigger systems is to reduce the rate to a more manageable 100 Hz while maintaining a highly efficient selection for rare signal processes. Even at the initial luminosity of $\mathcal{L} = 10^{31} \text{ cm}^{-2}\text{s}^{-1}$ it will be a challenge to keep the trigger highly efficient for all important final states while reducing the event rate.

The trigger consists of three levels. Level 1 (L1) is a hardware only system, with a latency of $2.5 \mu\text{s}$, that uses only coarse calorimeter and muon system information to reduce the event rate to a maximum of 75 kHz. Levels 2 (L2) and Event Filter (EF) are software based systems collectively known as the High Level Trigger (HLT) which serve to further reduce the rate to 2 kHz and 100 Hz, with latencies of 10 ms and 1 s respectively. L2 two has access to the full detector granularity information in Regions of Interest (RoIs) identified by L1 as well as the inner detector information. The EF makes use of the offline reconstruction algorithms within L2 RoIs with access to the full detector granularity information in these RoIs, and to better refined detector calibration and alignments [32], [33].

In principle, the high mass dilepton/diphoton resonance search should have a fairly straightforward trigger strategy as there are very high energy leptons in the event. However, there are several questions that remain:

- What trigger requirements are optimal for the analysis? What p_T thresholds and object quality selection should be applied?
- How can one estimate the trigger efficiency from data for such rare (or non-existent) events?
- Are the same object quality requirements that are appropriate from 'lower' p_T objects appropriate for very high energy objects?

This section addresses these questions, evaluates the trigger efficiency for the signal samples of interest, and discusses the trigger strategy for the earliest running periods of the ATLAS detector. This section is organized according to objects used to trigger the events.

4.2 Electron and Photon Triggers

Electron and photon candidates are accepted based on calorimeter information within a 4×4 sliding window of trigger towers that have an $\eta - \phi$ granularity of 0.1×0.1 . At this stage a combined EM-Tau trigger is used to select electrons, photons and tau leptons. At L2 and above electron and photon triggering diverges. Electron selection is based on shower shape information from the electromagnetic calorimeter and leakage into the hadronic calorimeter, as well as associated track information from the inner detector.

In 12.0.X the photon high level trigger (HLT) relies entirely upon calorimeter information and requires much tighter shower shape cuts than those used for electrons. In future releases inner detector tracking information will be added to identify photon conversion points at the EF stage. All the HLT algorithms use η dependent variables and the selection cuts differ across the η regions.

The Data Samples used for the analysis can be seen in reference 2, while the trigger menus configured in 12.0.6 in reference [34].

4.2.1 Efficiencies and normalizations

In order to study the trigger efficiencies alone and avoid convoluting its effects with detector acceptance and offline reconstruction efficiencies, we first normalize to a subset of 'good' events. The normalization

criteria adopted from [35]. Basically, it includes kinematical cuts, where a cut in η is applied to remove any detector acceptance effects, and a series of cuts based on a combination of shower shape and tracking variables, useful to discriminate electrons and photons from jet backgrounds in offline reconstruction.

4.2.2 Object based efficiencies

The exotics samples studied here are characterized by very high p_T electrons and photons. An interesting preliminary study is to examine their efficiencies of passing the triggers on an object basis. i.e. determining the efficiency for individual electrons and photons to pass a given trigger signature. Efficiency as a function of p_T is defined as:

$$Efficiency = p_T(N_1)/p_T(N_2), \quad (5)$$

where N_1 are the number of e/γ objects that survive the loose normalization and that give a trigger signature pass to a given trigger level and all its precursors, and N_2 are the number of e/γ objects that survive the loose normalization. e60 object efficiencies in $G(500\text{GeV}) \rightarrow e^+e^-$ using this normalization can be seen in Figure 29, and similarly for g60 in $G(500\text{GeV}) \rightarrow \gamma\gamma$ in Figure 30.

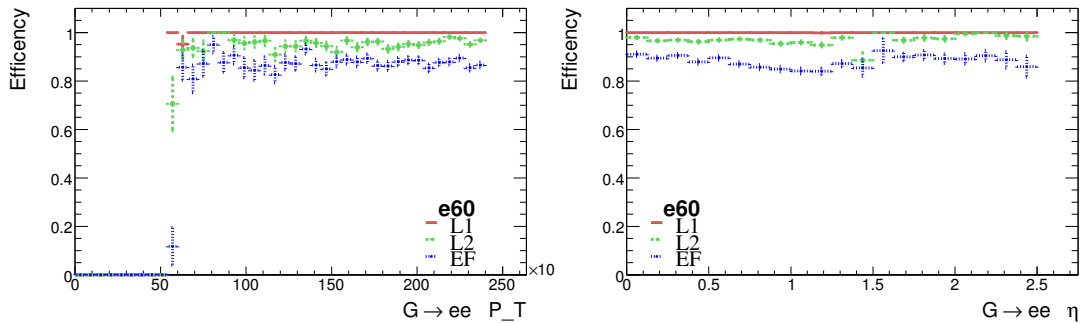


Figure 29: $G(500\text{GeV}) \rightarrow e^+e^-$ e60 efficiencies as a function of p_T (left), η (right).

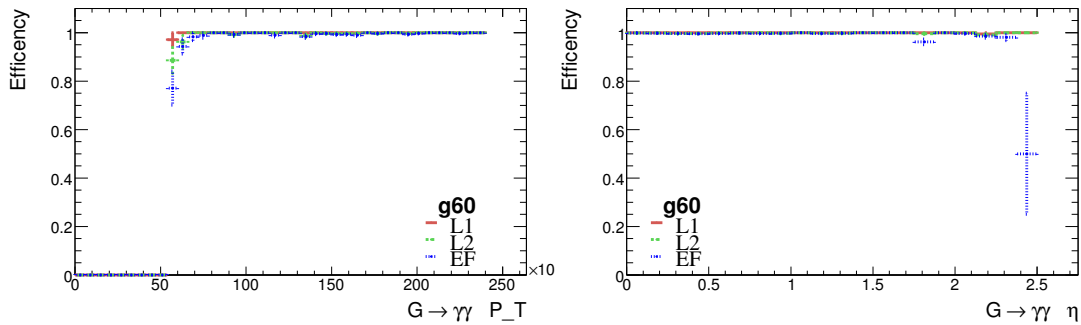


Figure 30: $G(500\text{GeV}) \rightarrow \gamma\gamma$ g60 efficiencies as a function of p_T (left) and η (right)

4.2.3 Event based Efficiencies

In order to study the trigger effects and not any reconstruction or acceptance effects, the sample is normalized to a subset of good events using the loose e/γ normalization with a p_T cut defined as the threshold,

and then the efficiency is computed as follows as:

$$Efficiency = N_3/N_4, \quad (6)$$

where N_3 is the number of events with at least one(two) e/γ objects that pass the e/γ loose normalization and that give a trigger signature pass to a given trigger level and all its precursors; and N_4 is the number of events with at least one(two) e/γ objects that survives the loose e/γ normalization. Event efficiencies can be seen in table 8 for $G(500\text{GeV}) \rightarrow e^+e^-$ and in table 9 for $G(500\text{GeV}) \rightarrow \gamma\gamma$, both with a loose e/γ normalization. These high p_T triggers should not have a prescale in the $\mathcal{L} = 10^{31} \text{ cm}^{-2}\text{s}^{-1}$ [36].

Signature	L1	L2	EF
$e60$	99.9 ± 0.0	95.8 ± 0.2	90.8 ± 0.3
$e25i$	85.9 ± 0.3	82.8 ± 0.4	80.9 ± 0.4
$2e15$	99.9 ± 0.1	84.8 ± 0.5	72.6 ± 0.6
$2e15i$	59.1 ± 0.7	50.9 ± 0.7	43.9 ± 0.7

Table 8: $G(500\text{GeV}) \rightarrow e^+e^-$ event trigger efficiencies with loose e/γ normalization

Signature	L1	L2	EF
$g60$	100.0 ± 0.0	99.8 ± 0.1	99.7 ± 0.1
$2g20$	100.0 ± 0.0	100.0 ± 0.0	99.5 ± 0.1
$2g20i$	70.1 ± 0.9	70.1 ± 0.9	69.8 ± 0.9

Table 9: $G(500\text{GeV}) \rightarrow \gamma\gamma$ event trigger efficiencies with loose e/γ normalization

4.2.4 Effect of the trigger on invariant mass distributions

As the gravitons were simulated with a mass of 500 GeV, we expect the reconstructed invariant mass distribution from the final state particles to be close to that value. Figure 31(a) shows the invariant mass distributions reconstructed after each trigger level, while Figure 31(b) shows the distributions only for the events that were accepted by 2g20i-2g20 trigger menus. The distributions for the other trigger menus were also done, and in all cases Offline distributions are peaked at 500 GeV, as well as those at L1, where a calibration factor was applied. At L2 and EF, the distributions are shifted and recalibration would be needed.

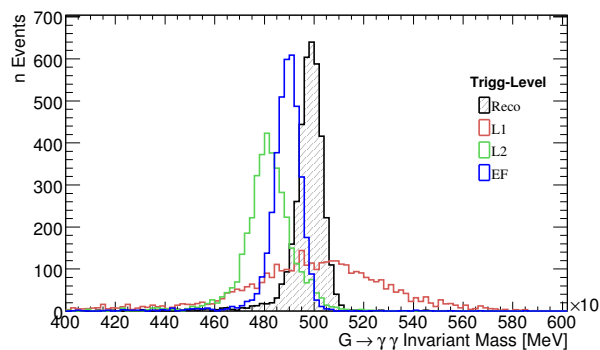
The effect of the isolation at L1 can be also appreciated in Figure 31(b) by comparing the relative height of the peaks between the plots.

The cuts corresponding to 12.0.6 trigger menus do not bias the invariant mass.

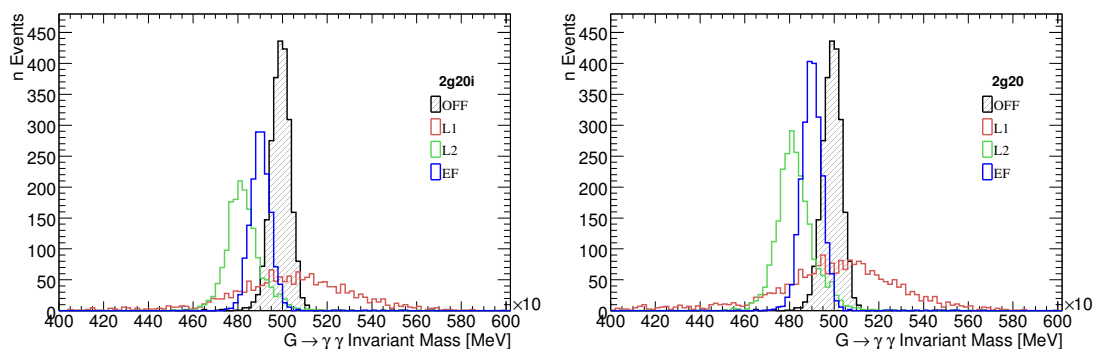
4.2.5 Current trigger configuration and strategy with early data

By looking at the tables 8 and 9 it is clear that the current trigger selection for high p_T dielectron/diphoton exotic decays can be implemented by any of the triggers without isolation. Double triggers as $2\gamma 20$ or $2e15$ can also be implemented for the high luminosity regimen without prescale giving good overall signal efficiencies.

Some new trigger menus will be available for new releases and many of them will have impact on exotics channels. The general strategy for the early running will include higher p_T thresholds with the



(a) All events



(b) Accepted events

Figure 31: $G(500\text{GeV}) \rightarrow \gamma\gamma$ invariant mass distributions reconstructed after each trigger level (a) for all the events, (b) only for the events accepted by 2g20i (left) 2g20(right) trigger menus.

possibility of implementing a pass-through HLT, which will be very useful for exotics analysis since almost all of the events will be stored. Prescaled unisolated triggers, and double object triggers will also be relevant. There are still many things to do mostly on deciding which will be the criteria to tag these dilepton/diphoton events.

<i>Sample</i>	Mu20 Efficiency (L1/L2/EF) %			Total Trigger Efficiency %
400 GeV ρ_T/ω_T	97.6 ± 0.10	98.8 ± 0.07	99.5 ± 0.05	96.0 ± 0.13
600 GeV ρ_T/ω_T	98.1 ± 0.08	98.5 ± 0.08	99.2 ± 0.06	95.9 ± 0.13
800 GeV ρ_T/ω_T	97.6 ± 0.10	98.7 ± 0.07	99.2 ± 0.05	95.6 ± 0.13
1 TeV ρ_T/ω_T	97.6 ± 0.09	98.7 ± 0.07	99.2 ± 0.05	95.6 ± 0.12
1 TeV Z' (SSM)	??	??	??	??
1 TeV Z' (E6)	97.8 ± 0.09	98.9 ± 0.06	99.5 ± 0.04	96.3 ± 0.1
2 TeV Z' (SSM)	97.6 ± 0.14	98.7 ± 0.11	98.9 ± 0.10	95.3 ± 0.2

Table 10: Simulated Trigger Efficiencies of Dimuon Resonance Samples

4.3 Muon Triggers

The ATLAS muon trigger is described in the technical design report [25]. A trigger menu has been proposed for both periods [31]. It is expected that during both running periods there will be a unrescaled single muon trigger without an isolation requirement. We will show that as expected for any likely value of the p_T threshold this is expected to be a highly efficient trigger for a high mass resonance decaying into two muons. The two muon triggers we study here require a single muon with a p_T of 20 or 40 GeV.

4.3.1 Efficiency Estimate

We estimate the muon trigger efficiency using several different methods. The first method is to rely on the trigger simulation run as part of the standard ATLAS reconstruction software from a full GEANT detector simulation and an emulation/simulation of the ATLAS muon trigger. While this is the simplest and most direct method it relies completely on simulation techniques which are known to be somewhat more optimistic (better resolution, higher efficiency,...) than results from real data from previous experiments at the Tevatron and before. Therefore, we also estimate the trigger efficiency using methods which could be applied to real data.

The trigger efficiencies for the dimuon heavy resonance Monte Carlo samples are shown in table 10. The trigger efficiencies are calculated with respect to the offline event selection. Two combined muons (requiring a muon with a combined fit from both the muon spectrometer and inner detector) are required with:

- $|\eta| < 2.7$
- $p_T > 30$ GeV
- Track fit $\frac{\chi^2}{\text{D.O.F}} < 10$
- Inner Detector and Muon Spectrometer track match $\frac{\chi^2}{\text{D.O.F}} < 10$.

The trigger efficiency quoted is simply the fraction of events satisfying the offline requirements which also fired the corresponding trigger.

Figure 32 shows the LVL1 trigger efficiency with respect to offline reconstruction as a function of ϕ , η , and p_T . There are several features of the efficiency distributions. First, notice that the efficiency is lower in the barrel region than in the end-cap. This is due to the incomplete trigger coverage in the barrel with respect to the precision chambers. The presence of support structures and services lead to incomplete geometric acceptance of the detector. As discussed in [25], the algorithmic efficiency is about 99% for muons within the trigger acceptance. Secondly note the two dips in the efficiency as a

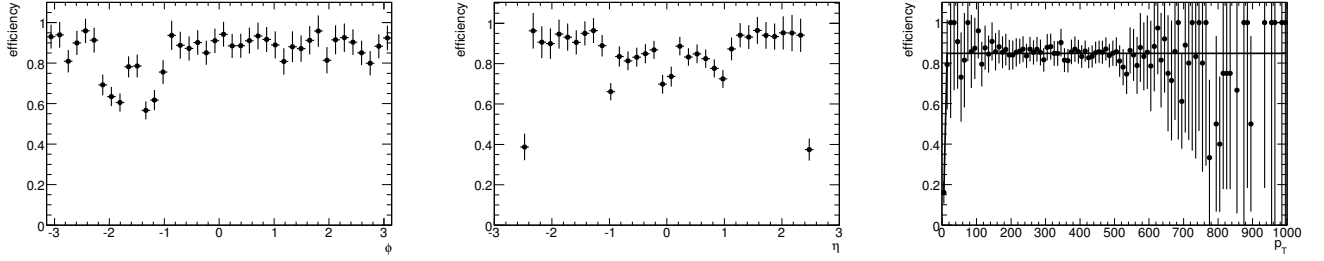


Figure 32: LVL1 trigger efficiency as a function of ϕ (right), η (center), and p_T with respect to offline event selection for the 1 TeV SSM $Z \nu$ sample .

function of phi. This is caused by the presence of the 'feet' support structure which leads to incomplete trigger coverage. Finally, note that the trigger chambers cover the region of $|\eta| < 2.4$ while the CSC (cathode strip chambers) allow offline muon reconstruction up to η of 2.7.

The efficiency as a function of p_T has been fit to a function parameterizing the efficiency as a function of transverse momentum. Since the estimated muon momenta has a finite resolution one expects the estimate to be Gaussian distributed about the true muon momentum. Thus by selecting the muons above a given threshold one is integrating the Gaussian distribution above some cut-off. The parameterization is written as:

$$f(p_T) = 0.5 \cdot A_2 \cdot (1.0 + \text{erf}(\frac{p_T - A_0}{\sqrt{2} \cdot A_1})) \quad (7)$$

where A_0 , A_1 , and A_2 are the fit parameters which represent, respectively, the p_T value at which the efficiency reaches half its maximum value, the slope of the turn-on curve, and the maximum efficiency in the plateau region. The statistical uncertainty on the trigger efficiency as a function of p_T can be written as :

$$\Delta f^2 = (\frac{\delta f}{\delta A_0})^2 \cdot (\Delta A_0)^2 + (\frac{\delta f}{\delta A_1})^2 \cdot (\Delta A_1)^2 + (\frac{\delta f}{\delta A_2})^2 \cdot (\Delta A_2)^2 \quad (8)$$

which is can be written:

$$\Delta f^2 = [\frac{A_2}{\sqrt{2\pi}A_1} \cdot e^{-\frac{(p_T - A_0)^2}{2 \cdot A_1^2}}]^2 (\Delta A_0)^2 + [\frac{A_2 \cdot (p_T - A_0)}{\sqrt{2\pi}A_1^2} \cdot e^{-\frac{(p_T - A_0)^2}{2 \cdot A_1^2}}]^2 (\Delta A_1)^2 + [0.5 \cdot (1.0 + \text{erf}(\frac{p_T - A_0}{\sqrt{2} \cdot A_1}))]^2 (\Delta A_2)^2 \quad (9)$$

where ΔA_0 , ΔA_1 , and ΔA_2 are the statistical uncertainties on the fit parameters.

There are several possible methods to evaluate the trigger efficiency from the data itself. A possible scheme is to look at the the trigger efficiency for a known experimentally clean signature that is similar to the final state of interest. In this case the only natural choice is to examine the trigger efficiency of the $Z \rightarrow \mu\mu$ final state. Here one can obtain a very clean signature which is very similar to the hypothetical heavy resonance (the difference being the mass of the resonance). Since the Z boson is 'light' compared to the total center of mass energy it can be produced with a significant p_T distribution. One can then measure then measure the trigger efficiency on the Z boson sample and extrapolate to high transverse momentum. The appeal of the method is that it uses data itself to measure the trigger efficiency which is *the* most accurate method of measuring the Z boson trigger efficiency. However, the method does come with caveats. The muon trigger efficiency is being extrapolated up to a factor of 10 higher transverse momenta then the mean of the muons from the Z boson decay. It is hoped that by checking the efficiency using several different methods the most accurate estimate can be achieved.

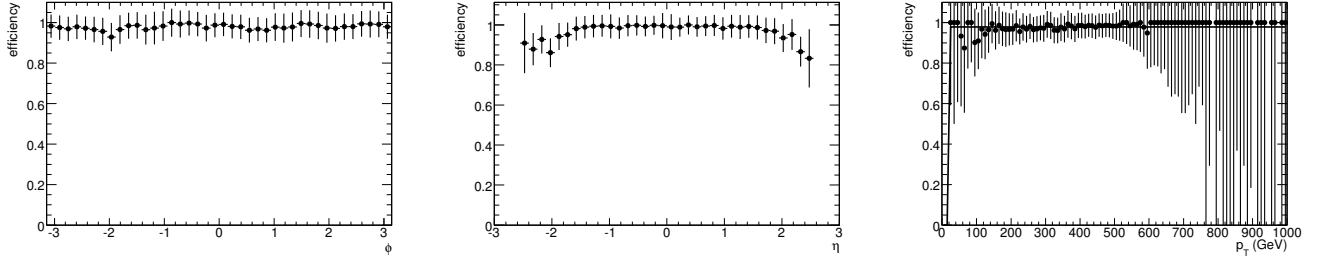


Figure 33: LVL2 trigger efficiency as a function of ϕ (right), η (center), and p_T with respect to offline event selection for the 1 TeV SSM Z' sample .

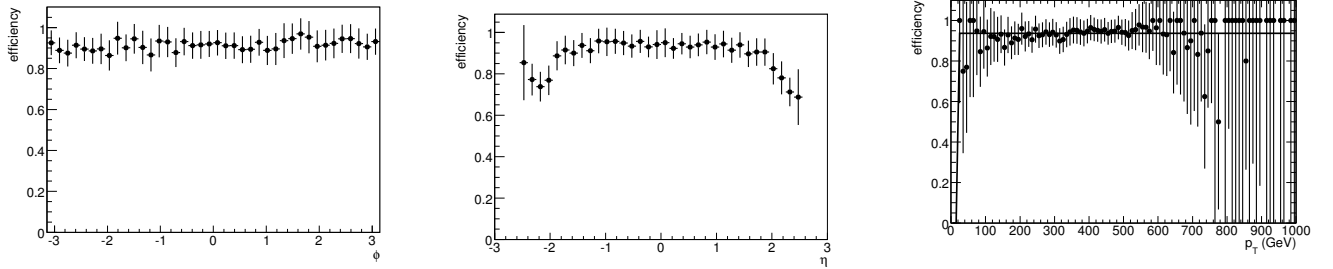


Figure 34: EF Trigger Efficiency as a function of ϕ (right), η (center), and p_T with respect to offline event selection for the 1 TeV SSM Z' sample .

The strategy of evaluating the trigger efficiency from data is as follows. First, use one of several methods to estimate the muon trigger efficiency as a function of the muon p_T and its uncertainty. Knowing the single object trigger efficiency then one can construct the probability for an event with N objects to pass the trigger. This can be written as:

$$P = 1 - \prod_{i=1}^N (1 - P_i) \quad (10)$$

where P_i is the object for the i th object to pass the trigger.

Two common ones that have been used extensively at the Tevatron are :

- Selection by orthogonal triggers.
- 'Tag and Probe' methods using the $Z \rightarrow \mu\mu$ decay.

The 'Tag and Probe' method is a simple method of using the known Z boson resonance as a 'standard candle' to measure high p_T lepton properties. The method proceeds by requiring two offline muons which have an invariant mass within several sigma of the known Z boson mass. Here we require the two offline muons have an invariant mass within 12 GeV of 91.1 GeV. So that the event be recorded in the first place we require that at least one of the muons satisfied the trigger requirement. In order to avoid any biases one muon is randomly assigned as the 'tag muon' while the other becomes the 'probe'. One then evaluates checks to see if the probe muon has passed the muon trigger. The efficiency obtained from the tag and probe method for the LVL1 component of the MU20 is shown in figure 35.

The efficiency as a function of the offline muon is fit according to equation 7. This procedure was repeated for all three trigger levels. The results are summarized in table 11. Note that all of the efficiency

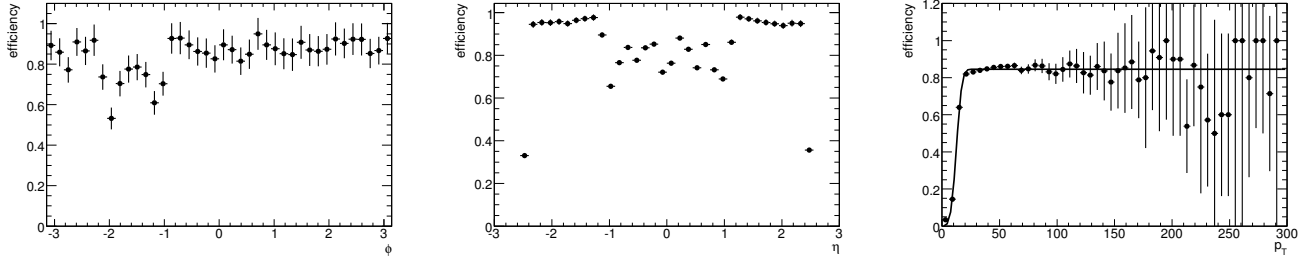


Figure 35: LVL1 trigger efficiency as a function of ϕ (right), η (center), and p_T with respect to offline event selection .

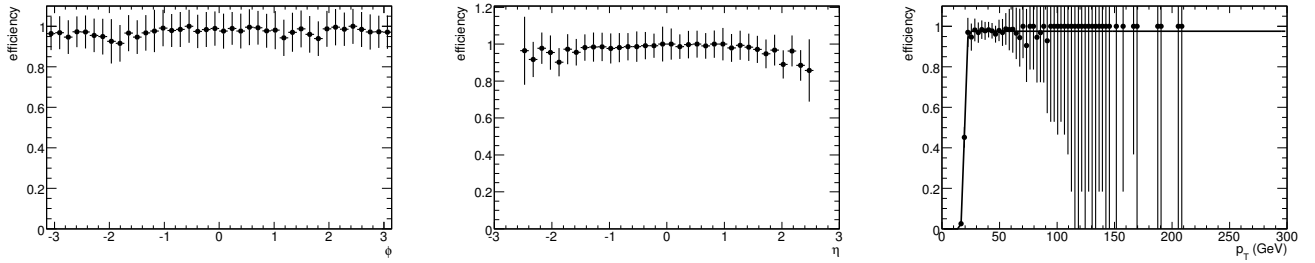


Figure 36: LVL2 trigger efficiency as a function of ϕ (right), η (center), and p_T with respect to offline event selection .

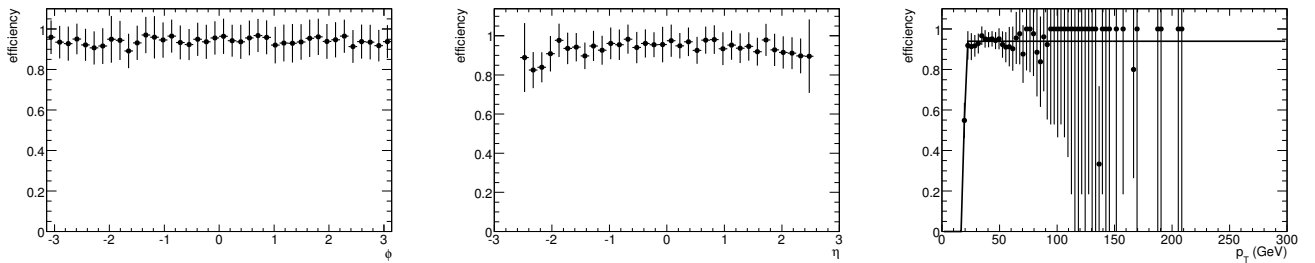


Figure 37: EF trigger efficiency as a function of ϕ (right), η (center), and p_T with respect to offline event selection .

Trigger Level	A_0	A_1	A_2
LVL1	12.5 ± 0.3	3.7 ± 0.4	0.845 ± 0.02
LVL2	19.6 ± 0.2	1.59 ± 0.19	0.976 ± 0.02
EF	19.5 ± 0.4	1.56 ± 0.3	0.931 ± 0.01

Table 11: Parameter values for the LVL1, LVL2, and EF of the muon trigger p_T trigger turn on

<i>Sample</i>	L1Mu20 Efficiency %	L2Mu20 Efficiency %	EFMu20 Efficiency	Total Efficiency
$Z' \ 1 \text{ TeV (SSM)}$	97.7 ± 0.11	99.0 ± 0.07	99.6 ± 0.04	96.3 ± 0.01
$Z \rightarrow \mu\mu$	97.83 ± 0.04	98.86 ± 0.03	99.52 ± 0.02	96.26 ± 0.05

Table 12: L1Mu20 trigger efficiencies at LVL1, LVL2, and Event Filter w.r.t offline reconstruction using orthogonal trigger selection to record events

plots shown above are not event efficiencies but rather for one of the muons from the Z . The probability that the event pass the trigger is significantly higher because the single muon trigger requires at least one muon to pass the trigger while each event has two offline muons. The LVL1 trigger efficiency is quoted with respect to the offline reconstruction. The LVL2 trigger efficiency is quoted with respect to the events which passed the LVL1 trigger and the EF with respect to events that passed both the LVL1 and LVL2 trigger.

In order to cross-check the two methods we take the parameterized efficiency as a function of p_T (averaged over ϕ and η) and apply the parameterization derived from the $Z \rightarrow \mu\mu$ sample to the signal sample offline muons. Then equation 10 is used to evaluate the probability that the event would have fired the MU20 trigger. These trigger probabilities are then averaged over all of the signal events and compared to the fraction of events that pass the simulated trigger.

By looking at events that were triggered by other signatures that are independent of the muon trigger one can select an unbiased sample. The offline reconstruction and event selection can then be applied. Finally, one can then look at the muon trigger decision and see what fraction of the events passed the corresponding muon trigger. For dimuons - a natural orthogonal trigger to use for this method would be a track based trigger. However, this cannot be used at LVL1 since there is no LVL1 track trigger. The only available triggers at LVL1 are the muon and calorimeter based triggers. In order to cross-check the previous two methods we first look for events that have passed the single 20 GeV jet trigger. We then perform the offline analysis and require that we have a dimuon pair following the same procedure for offline identification as above. We then look at the fraction of events which passed the LVL1, LVL2, and EF trigger conditions. The results are are tabulated in table 12 and are in good agreement with the other two methods. In the real experiment, a single jet trigger of 20 GeV would be very highly prescaled and hence will suffer from very poor statistics. One could in principle use events that passed any calorimeter trigger for this study - however then one must be careful to account for biases in the event topology. Such as study is beyond the scope of this note and we use the tag and probe method as the primary results and only quote the orthogonal signature study as a cross-check.

4.4 Tau Triggers

The tau lepton decays to hadronic states in 65% of the cases, and the rest of time to lighter leptons (e or μ). In our studies of di-tau final states we select events triggered with a single lepton (e/μ) trigger. Thus, we consider two true final states, which we denote $e\tau_h$ and $\mu\tau_h$. In this section we present performance of the electron and the muon triggers based on trigger decision at the Event Filter level (EF). Details about MC sample used in the analysis are given in section 2.

For $e\tau_h$ channel we consider two trigger menus called e25i and e60 described in section 4.2, which are designed to select events with p_T of the electron above 25 GeV and 60 GeV, with and without isolation in the calorimeter required respectively. The $\mu\tau_h$ events are selected using trigger menu called μ 20 described in section 4.3, appropriate for selection of muons with $p_T > 20$ GeV - without an isolation requirements. Figure 38 shows the efficiency of the trigger as a function of p_T , η and ϕ . For the $e\tau_h$ channel we observe

- A drop of efficiency for e25i menu with p_T due to requirement of isolation in the calorimeter. Therefore to improve efficiency we focus on events selected by either e25i or e60 trigger menu.
- Some number of events triggered by e60 with p_T of an electron below the menu threshold. Those events correspond to the other tau in the event passing all the cuts designed in e60 menu.
- A Drop in efficiency around $|\eta|=1.5$ due to end-cap/barrel crack in the calorimeter.

The trigger for the $\mu\tau_h$ channel is less efficient in the barrel region due to the designed support structure, is particular around $\eta=0$ corresponding to the crack region in the muon chamber and less efficient between $\phi=-1.0$ and $\phi=-2.2$ corresponding to the 'feet' regions.

Trigger menu	e25i	e60	e25i e60	mu20
Efficiency wrt to truth	(71.9±0.8)%	(77.8±0.9)%	(79.2±0.7)%	(75.6±0.7)%
Nevts for 1fb	412	292	454	446
Efficiency wrt offline	(75.9±0.7)%	(80.7±0.8)%	(83.7±0.6)%	(72.4±0.8)%

Table 13: Trigger efficiency for different trigger menus for taus from Z' with $e\tau_h$ and $\mu\tau_h$ final states.

Table 13 summaries the efficiency of the trigger. The first row gives the efficiency normalized to all events passing relevant kinematic cuts³⁾, second presents expected number of events for 1 fb^{-1} of data from $Z' \rightarrow \tau\tau$ selected by respective trigger menu and the last column shows the efficiency normalized to all events selected for offline analysis⁴⁾ which pass adequate kinematic cuts³⁾.

³⁾Events inside $\eta < 2.5$ passing a p_T cut used at the EF. For either e25i or e60 menu, the p_T cut at 25 GeV was used.

⁴⁾Electrons were identified offline with the loose criteria, whereas muons were required to pass a cut on $\chi^2 < 20$ as described in Sec.3.1 and Sec. 3.2 respectively

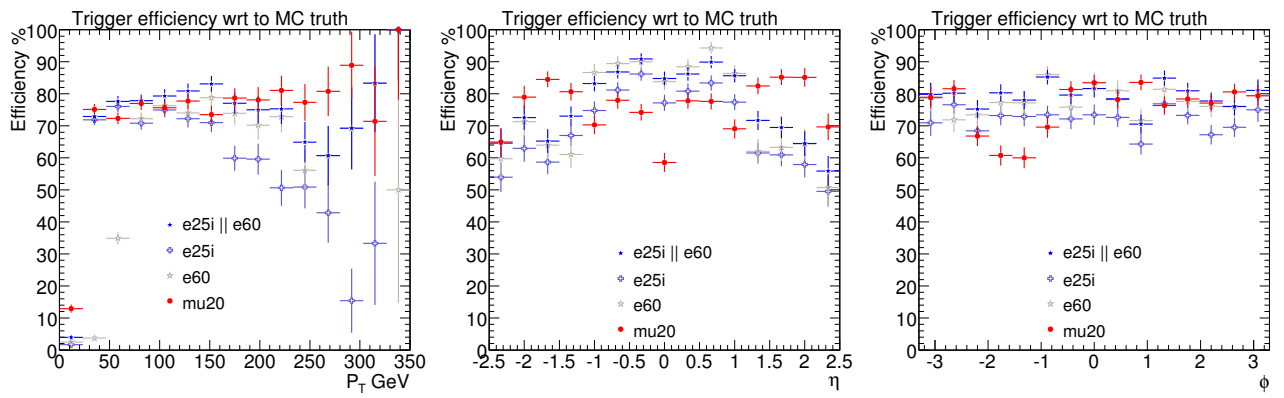


Figure 38: Efficiency as a function of p_T (left), η (center), and ϕ (right) for taus from Z' with $e\tau_h$ and $\mu\tau_h$ final states.

5 Uncertainties and backgrounds

In this section, we investigate the Standard Model and setup limits on its uncertainties to be used in the Exotic searches.

5.1 Dileptons

5.1.1 Theoretical uncertainties

PDF Uncertainties The precision of the Standard Model prediction for the dileptonic cross-section at the LHC is limited by uncertainties in Parton Distribution Functions (PDF). The measured cross-section σ_X for any given event with the momentum transfer Q depends on the parton distribution functions f for parton a and b with flavour $flav$, each carrying the momentum fraction x , as follows [37]:

$$\sigma_X = \sum_{a,b} \int_0^1 dx_a dx_b f(x_a, flav_a, Q^2) f(x_b, flav_b, Q^2) \times \sigma_{ab \rightarrow X}(x_a, x_b, Q^2) \quad (11)$$

where $\sigma_{ab \rightarrow X}$ is the partonic cross-section. Different collaborations like CTEQ [38], MRST [39] and ZEUS [40] extract PDFs from experimental data (figure 39). In this study the CTEQ61 PDF uncertainty

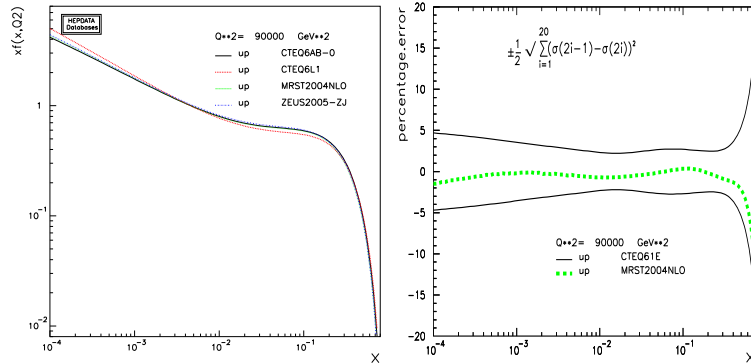


Figure 39: Left: Up distribution for CTEQ61, CTEQ61, MRST2004NLO and ZEUS2005-ZJ at $Q^2 = 90kGeV^2$. Right: A comparison between the CTEQ uncertainties on that up distribution and the MRST central value.

sets are used throughout the analysis which reflect recent input data from deep inelastic scattering (DIS) at HERA as well as both proton-antiproton collisions and fixed target experiments at the Tevatron. A detailed description of further input data and used methodology can be found in [38]. Further PDF sets used in this study are MRST2004NLO [39], ZEUS2005NLO [40] and CTEQ61 [38]. They are based on NLO fits. Unfortunately, there are significant uncertainties in the experimental measurements used to determine PDFs. Some of these uncertainties are strongly correlated. The most correct treatment of these correlations is still the subject of current research. Also, there are uncertainties in the assumptions about the underlying theoretical model. These include assumptions about the non-perturbative part of the parton model as well as limitations in QCD calculations.

The analysed data set is a fully simulated Drell-Yan dielectron final state requiring the invariant mass of the two electrons to be greater than 150 GeV. The CTEQ61 parton distribution functions - which have been generated with a leading order fit and with a leading order strong-coupling constant α_S - have been used for the production of this sample with Herwig [41] and Jimmy [42]. Available computing power does not allow regeneration of all data samples according to PDF uncertainties. Thus, it is necessary to

reweight the analysed events generated with set *PDF1* according to set *PDF2*. This is, however, only possible for the hard process. The new weight is given by:

$$Weight = \frac{f_a^{PDF2}(x_a, flav_a, Q^2) \times f_b^{PDF2}(x_b, flav_b, Q^2)}{f_a^{PDF1}(x_a, flav_a, Q^2) \times f_b^{PDF1}(x_b, flav_b, Q^2)}. \quad (12)$$

In this analysis, the hard process generated with leading-order PDFs was weighted by the central values of the next-to-leading order CTEQ61 PDFs. The uncertainty on the resulting distribution was evaluated by reweighting the events to the 40 corresponding error sets provided by the CTEQ collaboration. PDF sets are calculated by minimising a global χ^2 function which contains the experimental data and the underlying model. The errors on the resulting theoretical parameters - 20 in the case of CTEQ - are obtained using the inverse of a single Hessian matrix expressing the variation of the χ^2 with respect to both theoretical and systematic offset parameters. By iteratively diagonalising the Hessian matrix 40 eigenvectors, two for each dimension of the parameter space, are obtained. Each of them describes the PDF uncertainty from a certain combination of measurements. Thus, the error sets describe the neighbourhood of the minimum in the 20-dimensional PDF parameter space. A detailed description can be found in [38]. The 20 pairs of error sets are independent by construction. Thus, it is necessary to combine the relative uncertainties quadratically. Special care has to be taken with asymmetric error sets. In this study the uncertainties have been added as follows:

$$\sigma^+ = \sqrt{\sum_{i=1}^{20} [\max(\sigma_i^+, \sigma_i^-, 0)]^2} \quad (13)$$

$$\sigma^- = \sqrt{\sum_{i=1}^{20} [\max(-\sigma_i^+, -\sigma_i^-, 0)]^2} \quad (14)$$

Here, σ_i^\pm is defined as the relative difference of the histogram with the reweighted histogram h_i and the central value h_0 :

$$\sigma_i = \frac{h_i - h_0}{h_0}. \quad (15)$$

As can be seen in Figure 40 the overall cross section uncertainty up to an invariant mass of 1000 GeV is between 4 and 8%. The uncertainties in Y , shown in Figure 41, are most significant in the central region of the detector. The uncertainty on the production cross-section is greatest (7%) at large values of rapidity. This is due to the fact that at least one quark needs to have a fairly large x in order to create a dilepton pair in this region of the phase space. PDFs are generally poorly constrained for large x above about 0.1 (figure 39). Furthermore, the impact of 40 different CTEQ error eigenvectors has been investigated. For low masses up to 400 GeV eigenvector 30 is the most significant one. For higher masses eigenvectors 21 and 7 become more important. Each eigenvector combines different information about certain parton distribution functions. More details about the different error eigenvectors can be found in [43]. Generally, estimated errors published by CTEQ are more conservative than errors given by MRST as the global χ^2 of the fit is increased by $\delta\chi^2 = 100$ for CTEQ [38] and $\delta\chi^2 = 50$ for MRST [44] to obtain the error matrix. Furthermore, the central values of ZEUS2005-ZJ and MRST2004NLO are almost consistent with the errors around the central value of CTEQ61 (figure 39) in the relevant region of x between 10^{-3} and 10^{-1} . Therefore, a sole analysis of uncertainties provided by CTEQ is considered to be sufficient.

NLO Effects In addition to differences between various collaborations, there is a significant difference in PDF sets, and thus in the invariant mass distribution, depending on whether the hard matrix elements that enter into the perturbative QCD calculations are leading-order (LO) or next-to-leading-order (NLO).

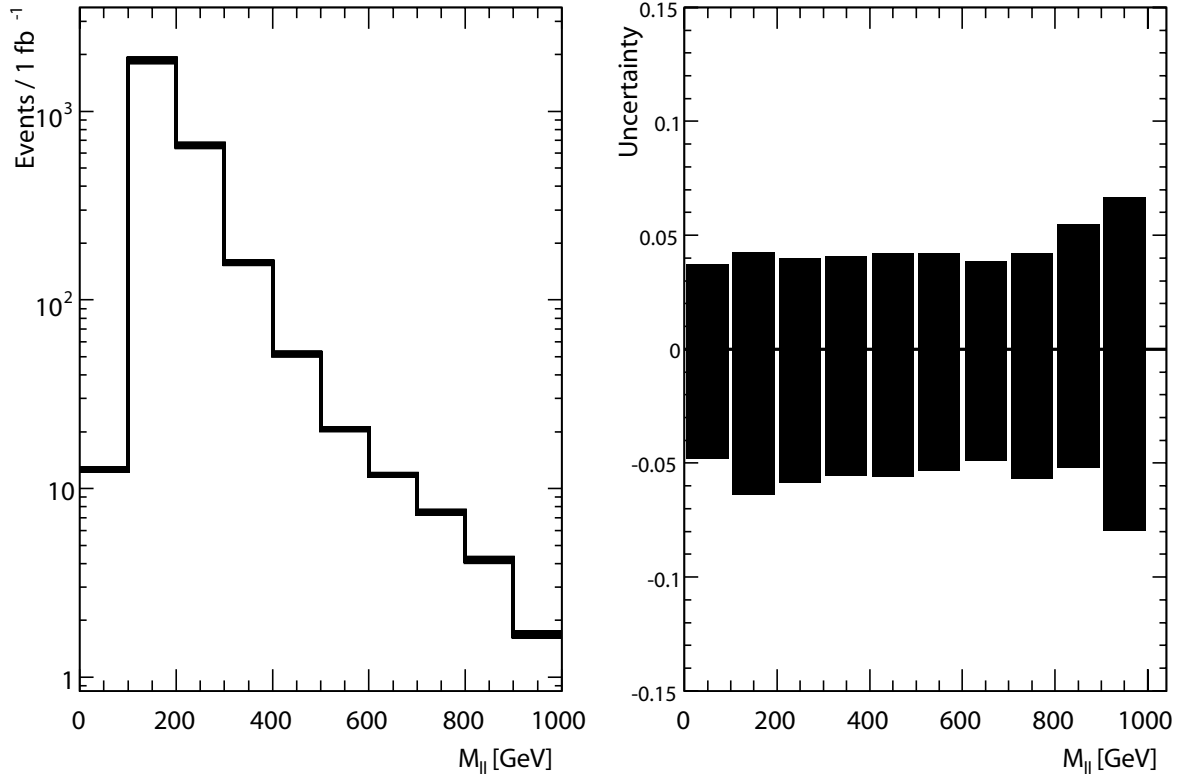


Figure 40: Left: Forty-one invariant mass distributions up to 1 TeV after reweighting for high-mass Drell-Yan dielectron final state. Right: Overall uncertainty on the high-mass Drell-Yan distribution after quadratically adding all uncertainties (Eq. 13 and 14).

The analysed data set has been generated with a LO-PDF set. In order to estimate this effect the analysed events have been reweighted to NLO PDF sets. In order to be consistent, also k-factors describing the change in cross-section between LO and NLO Monte Carlo had to be applied. The k-factors used for this analysis have been calculated by Amanda Cooper-Sarkar using a Fortran code [45] that calculates the Drell-Yan cross section $d\sigma/dYdM^2$ in proton collisions at the leading and next-to-leading order. The contribution from the s-channel Z exchange is included into the program. Various parton distribution sets can be used with this code. The k-factors used in this analysis have a granularity of 10 bins in the dilepton rapidity Y and 10 bins in the invariant mass M_{II} . As can be seen in Figure 42 NLO effects lead to an mass dependent increase in cross section of about 24 - 36%. figure 43 shows the change of Y distribution through NLO effects. For the following studies, the QCD NLO-corrections are approximated by a constant k-factor with systematic uncertainty of 5% to take into account the non constant part of the k-factor.

Hard Process Scale When performing calculations to determine the Drell-Yan cross-section one must specify renormalization and factorization Q^2 , μ_R and μ_F scales. The default scale was chosen to be $\mu = \sqrt{s}$. Most previous studies vary these scales up and down by a factor of two and take the variation as a conservative estimate of the the uncertainty introduced by this choice. Using public code provided

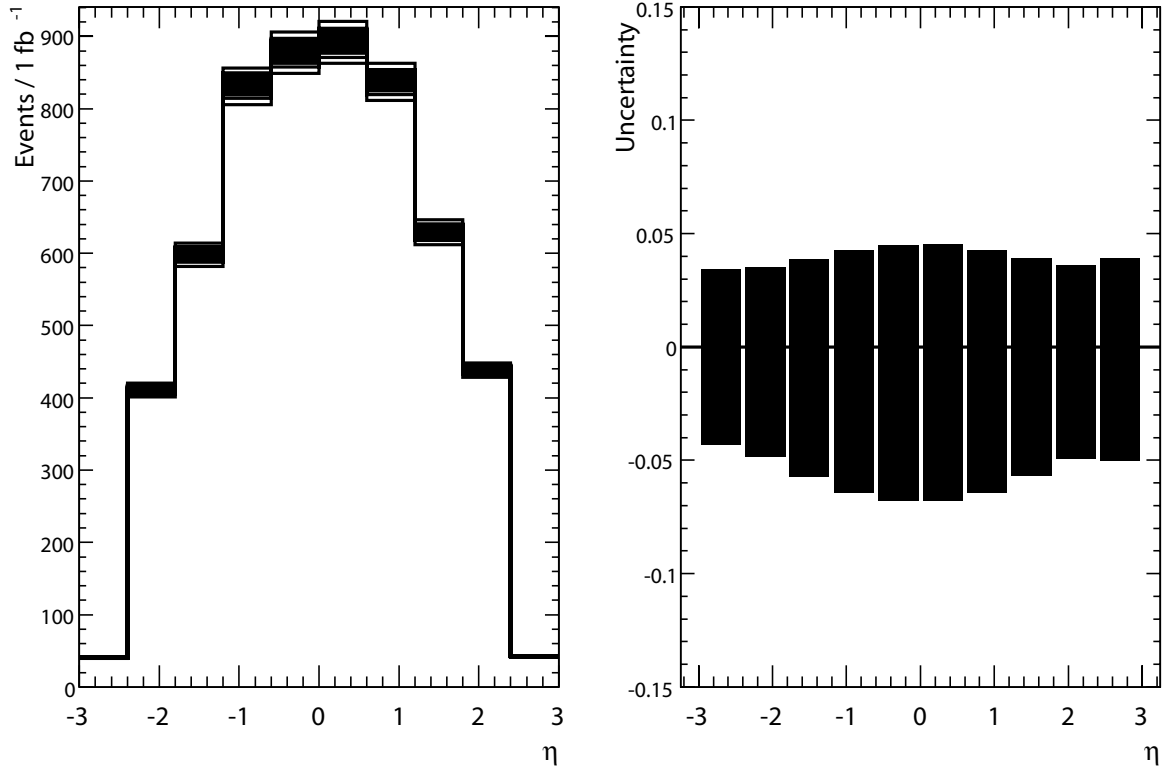


Figure 41: Left: Forty-one eta distributions after reweighting for high-mass Drell-Yan dielectron final state. Right: Overall uncertainty on the lepton η distribution after quadratically adding all uncertainties (Eq. 13 and 14).

by [46] we modify both scales and find a variation of around 1 % for invariant masses less than 1.5 TeV. These are consistent with previous studies [47]. In [47] they report that the scale uncertainty at much higher invariant masses (around 5 TeV significantly larger - up to 25 %) but this is far above the mass ranges considered in this study. In order to be conservative, a value of 3% is considered in the following studies.

5.1.2 Luminosity

After collection of the data, offline processing, and final event selection we obtain a total number of events and an estimate of the background contribution to our final data sample. In order to turn this into a cross-section or a limit on the cross-section we must know how much luminosity the data sample we are analysing corresponds to.

The event yield for a given process can be written simply as :

$$N = L \cdot \sigma \quad (16)$$

where N is the event yield, L is the integrated luminosity, and σ is the cross-section of the given process. Since the number of events for both signal and background depend on the integrated luminosity we must estimate the luminosity its uncertainty. Several methods have been proposed :

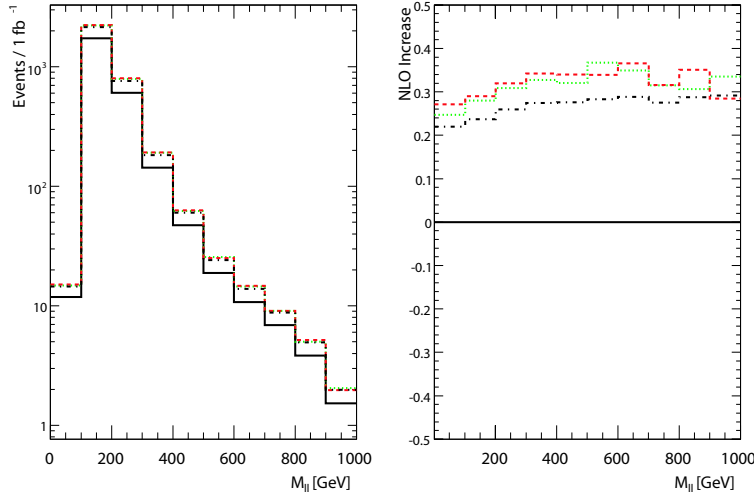


Figure 42: Left: Four invariant mass distributions up to 1 TeV after reweighting for high-mass Drell-Yan dielectron final state: CTEQ61l (LO, solid black), CTEQ61 (NLO, dashed-dotted black), MRST2004NLO (NLO, dotted green) and ZEUS2005-ZJ (NLO, dashed red). For the NLO PDF sets the distributions have also been reweighted with analytical k-factors describing NLO Monte Carlo. Right: The relative differences of the reweighted distributions compared to the original one: CTEQ61l (Solid black), CTEQ61 (Dashed-dotted black), MRST2004NLO (Dotted green) and ZEUS2005-ZJ (Dashed red).

- Luminosity estimate from measurement of beam parameters.
- Luminosity estimate from measurement using the optical theorem.
- Luminosity estimate from measurement of a process with precisely known cross section.

In this section we briefly discuss each method and its expected uncertainty.

The luminosity can be expressed as:

$$L = F \frac{f \sum_i N_1^i N_2^i}{4\pi \sigma_x^* \sigma_y^*} \quad (17)$$

where $F = 0.9$ is a factor to take into account the non-zero crossing angle of the LHC beams, $f = 11$ kHz is the beam-revolution frequency, N_1^i and N_2^i are the numbers of protons in the colliding bunches and σ_x^* and σ_y^* are the transverse bunch widths at the interaction point. By measuring these quantities one could calculate the luminosity. Unfortunately, at least initially this method is only expected to have an accuracy of 20% to 30% [48]. Therefore we consider this only as confirmation method.

The second method is one traditionally used at hadron colliders. By installation of very forward detectors one can measure the small-angle scattering. The optical theorem tells us that the luminosity can be extracted from the relation [49] :

$$L \frac{dR_{elastic}}{dt} \Big|_{t=0} = \frac{R_{total}^2 (1 + \rho^2)}{16\pi} \quad (18)$$

where L is the integrated luminosity, $\frac{dR_{elastic}}{dt} \Big|_{t=0}$ is the rate of forward elastic scattering (with square-momentum transfers t), R_{total} is the total rate of pp interactions, and ρ is the ratio of the real to imaginary

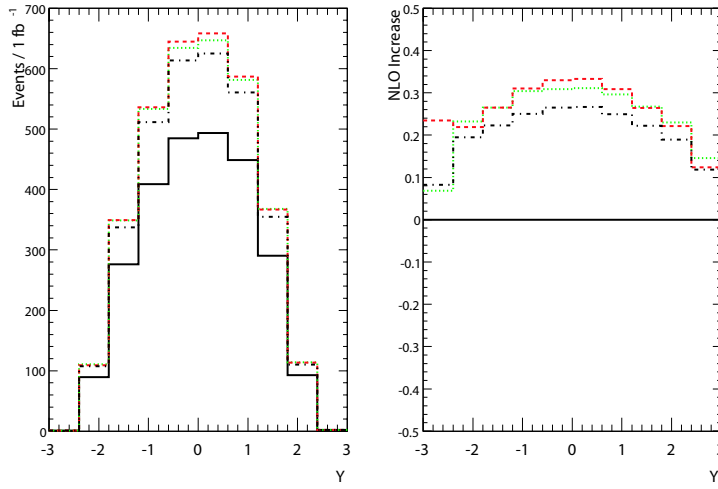


Figure 43: Left: Four Y distributions after reweighting for high-mass Drell-Yan dielectron final state: CTEQ6ll (LO, solid black), CTEQ61 (NLO, dashed-dotted black), MRST2004NLO (NLO, dotted green) and ZEUS2005-ZJ (NLO, dashed red). For the NLO PDF sets the distributions have also been reweighted with analytical k -factors describing NLO Monte Carlo. Right: The relative differences of the reweighted distributions compared to the original one: CTEQ6ll (Solid black), CTEQ61 (Dashed-dotted black), MRST2004NLO (Dotted green) and ZEUS2005-ZJ (Dashed red).

part of the elastic forward amplitude. Using the Roman Pot detectors ATLAS will measure the forward scattering while the total pp cross-section will be measured by Totem [50]. This method is expected to measure the luminosity to an accuracy of 5 to 10 % [49].

The final method of determining the luminosity from normalizing to a well known cross section. A number of processes have been discussed [49] - which focuses on two photon production of dileptons. In the case of the dilepton search one could measure the event yield in $Z \rightarrow ll$ events and normalize to the calculated cross-section which is known to a few percent. Further the overall normalization could also reduce the uncertainty to the absolute magnitude of the Drell-Yan background [49]. For the purposes of this note, we assume that in early running a nominal precision of 5 % can be achieved.

5.1.3 Summary of systematic uncertainties

We have made an attempt to estimate, based on theoretical inputs, results from other experiments, predictions from test beam, system designs, and Monte Carlo methods. However, it should be kept in mind that some of these numbers simply cannot be realistically estimated until data taking begins. Systematic uncertainties from higher order EW corrections and high x summation are beyond the scope of this note.

For the sensitivity studies, we have considered and agreed on the following systematics:

- k -factor of 1.35 with a 5% uncertainty
- 5% uncertainty on the luminosity
- 8% uncertainty on the PDF and 3% uncertainty on the renormalization/factorization scale
- 4% uncertainty on the energy scale.

6 Search for Exotic Physics

6.1 Introduction

In this section we present the discovery potential of several resonant signatures in the early running with ATLAS. We focus on the reach with an integrated luminosity of up to 10 fb^{-1} of data. The results presented here are updated feasibility studies to explore the discovery potential in the dilepton and diphoton final states with early data. The values of systematic uncertainties are those computed in the previous section. Exceptionally, some studies will use different values. In this case, the new used values are shown.

The statistical significance of an expected signal can be evaluated in several ways. The simplest approach, “Number Counting” is based on the expected rate of events for the signal and background processes. From these rates, and assuming Poisson statistics, one can determine the probability that background fluctuations produce a signal-like result according to some estimator; e.g., the likelihood ratio. In the “Shape Analysis” approach, a detailed knowledge of the expected spectrum of the signal for one observable ²⁾ can be used to improve the sensitivity of the search by treating each mass bin as an independent search channel, and combining them accordingly. The resulting sensitivity is in general higher than the estimation given in the Number Counting approach. In the Shape Analysis, the data is fitted or compared to two models: a background-only model and a signal-plus-background model. They are also called “Null Hypothesis”, noted H0 and “Test hypothesis”, noted H1, respectively. For each of the models, a log-likelihood or a χ^2 is computed and the ratio of the two log-likelihoods or the difference of two χ^2 s are estimated and used to compute the “Confidence Levels” noted CLs or significances, noted S. The input signal and background shapes are given to the fitting algorithms either as histograms in the non-parameterised approach [51] or as functions in the parameterised approach.

In the following, we will investigate Exotic dilepton or diphoton resonances using parametrized, non-parameterised and number counting methods. Only Z' in the dielectron and dimuon channels, Graviton in the dielectron, diphoton and ditau channels and Technicolor in the dimuon channel are investigated so far. This is an attempt to make template analyses of exotic models which can be studied at once, following their final state topology.

6.2 $Z' \rightarrow ee$ in the parameterised fit approach

When estimating the significance of a local excess of events, the size of the region considered, relative to the width of the expected resonance, may affect the sensitivity of the search [52]. This section presents an assessment of the size of this effect for the Z' dilepton searches. The above procedures, however, assume a good knowledge of the signal location and its cross section relative to the background. However, in the case of general dilepton searches, this is not the case; other than lower limits, there are no constraints on the mass of possible dilepton resonances, and their cross section and width vary among models. As a result, if an excess is found in the dilepton invariant mass, its significance will have to be evaluated in a way that takes into account the possibility of background fluctuations of different masses, cross sections and widths. One possible way to do this is through the use of maximum likelihood fits, where these quantities are free parameters.

Samples and selection: To estimate the effect on the sensitivity of the unknown rate and location of a dilepton resonance, the decay $Z'_{SSM} \rightarrow ee$ was generated for 16 true Z' masses between 1 and 4 TeV with a lower cut on the true dilepton mass of 0.5 TeV in all cases. Each sample was simulated and reconstructed using ATLFAST, and events were required to have two back-to-back leptons of opposite

²⁾for example: the invariant mass distribution may be used in the shape analysis

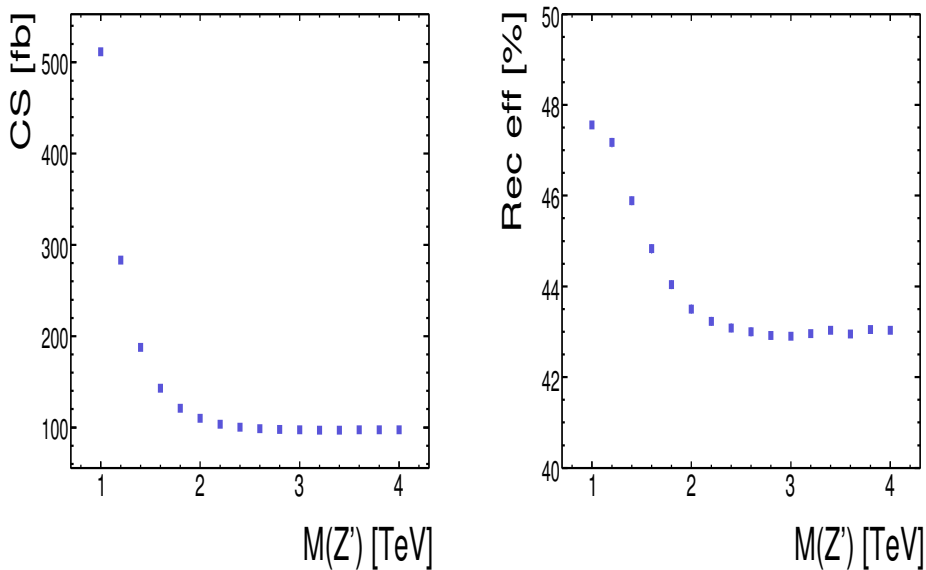


Figure 44: Cross section and reconstruction efficiency for the Z'_{SSM} , as obtained from the generator PYTHIA. The reconstruction efficiency includes the cuts described in the text.

charge with $P_T > 20$ GeV within $|\eta| < 2.5$. For an estimation of the expected background, Standard Model Drell-Yan production was used.

Figure 44 shows the cross sections and reconstruction efficiencies of the signal samples used. Since the aim is to study the effect of having an unknown resonance mass, all these samples were generated with the same lower bound for the Drell-Yan contribution (500 GeV); expectedly, as the mass of the Z' boson grows, and the cross section of the resonance decreases, the total cross section for the corresponding sample tends to a constant value (that of the falling part of the distribution). The plot on the right of figure 44 shows the reconstruction efficiency for the cuts mentioned above. An extra factor of 0.8 was added to account for the single-lepton reconstruction efficiency, assuming 90% per lepton.

Figure 45 shows the invariant mass distributions, after the cuts described, for true masses of 1, 2, 3, and 4 TeV, as well as the Drell-Yan fall. The plot on the right shows an amplification of the region around 1 TeV, showing the depletion of the spectrum due to destructive interference.

Fit-based approach In what follows, a simplified model is used to assess the effect of allowing the size and location of the signal float. The shape of the background model is fixed based on a fit to the reconstructed dilepton invariant mass for Standard Model $Z \rightarrow ee$ (figure 46).

The signal was modeled via the multiplication of a Breit-Wigner distribution (with mean m_0 and width Γ), and the function $\exp(-|m_{ll} - m_0|/6\Gamma)$. The absolute value in the exponential is used to limit the range of its effect on the low mass region of the background shape. Figure 47 shows the result of a binned maximum likelihood fit of this function to the 3 TeV Z' spectrum, after reconstruction cuts, together with the outcome of toy Monte Carlo experiments generated according to the signal plus background model (center) and to the background-only model (right plot). On top of each toy Monte Carlo histogram, the red line shows the (maximum-likelihood) fit to the signal-plus-background model; the green line corresponds to the background-only model.

In order to determine the significance of an expected signal at a given luminosity, a large number of toy Monte Carlo experiments is generated and fit to the two models H0 and H1 discussed above. The

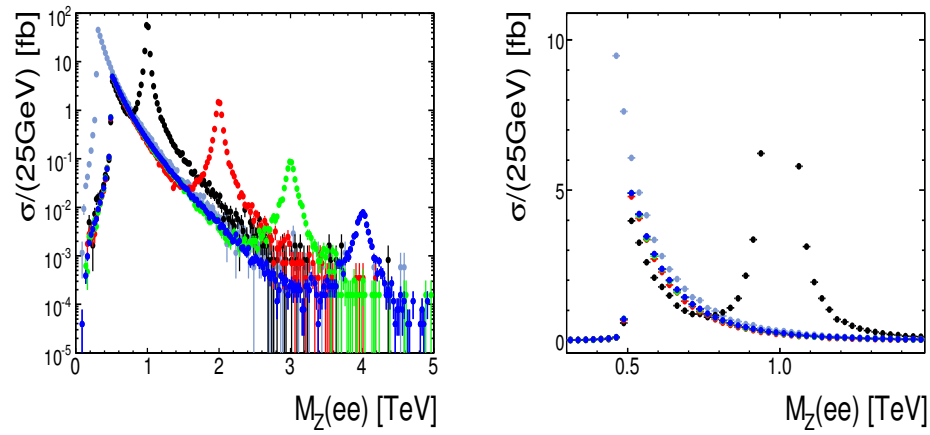


Figure 45: dielectron invariant mass distribution after the cuts described in the text. Right: zoom to the region around 1 TeV, showing the effect of interference with the Drell-Yan process.

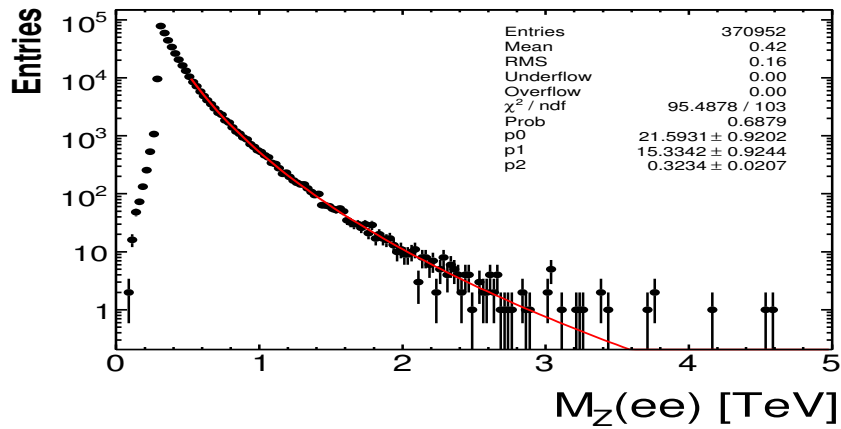


Figure 46: Fit used for the shape of the Drell-Yan background.

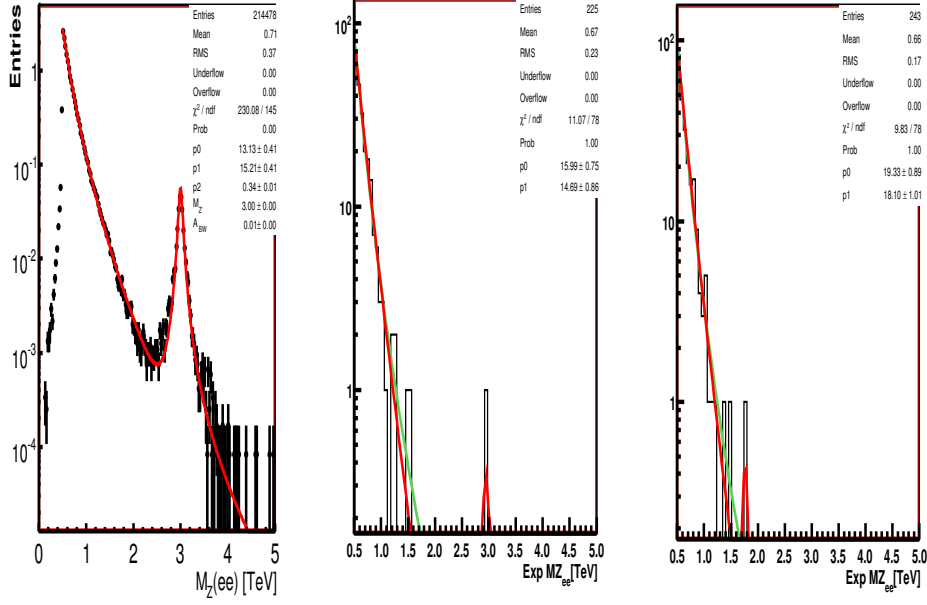


Figure 47: Left: fit to the reconstructed dilepton mass using the cuts described in the text. Center: fits to a Signal+Background (H1) toy Monte Carlo pseudoexperiment. Right: fits to a background-only (H0) pseudoexperiment.

resulting maximum likelihood distributions were then used to obtain the probability of a type II error, by obtaining the fraction of background-only pseudoexperiments whose likelihood ratio was larger than the median of the signal-plus-background likelihood ratio distribution. Figure 48 shows the likelihood ratio distributions for a 3 TeV Z'_{SSM} , corresponding to an integrated luminosity of $6.5 fb^{-1}$. On the left, in red, is the distribution of the log-likelihood ratio for fits to H0 pseudoexperiments. The plot in blue corresponds to fits to toy Monte Carlo pseudoexperiments generated according to the H1. One million outcomes were used for each distribution in order to estimate the fraction p of the H0 distribution that has a likelihood ratio larger than the mean of the H1 distribution. This tail is shown filled in red on the figure. The value of p is then transformed into significance following the convention under which $p = 2.9 \times 10^{-7}$ corresponds to 5 sigma. The fraction shown in the plot corresponds to a significance of 4.1 sigma.

Results A total of about 100 million toy Monte Carlo pseudoexperiments were generated and fit covering different masses, luminosities, and fit procedures. The method described above was used to estimate the expected significance on each case. The obtained results are compared to the Number Counting approach. The “Number Counting” uses a maximum likelihood estimator. The expected number of signal and background events, s and b were obtained from windows around the true value of the Z' mass; the size of the window was given by 2.5 times the expected width (including detector resolution). Assuming Poisson statistics, one determines the probability that background fluctuations produce a signal-like result, which is then transformed into the customary “number of sigmas” language via the inverse error function. Given an expected number of signal and background events, s and b , one can approximate the

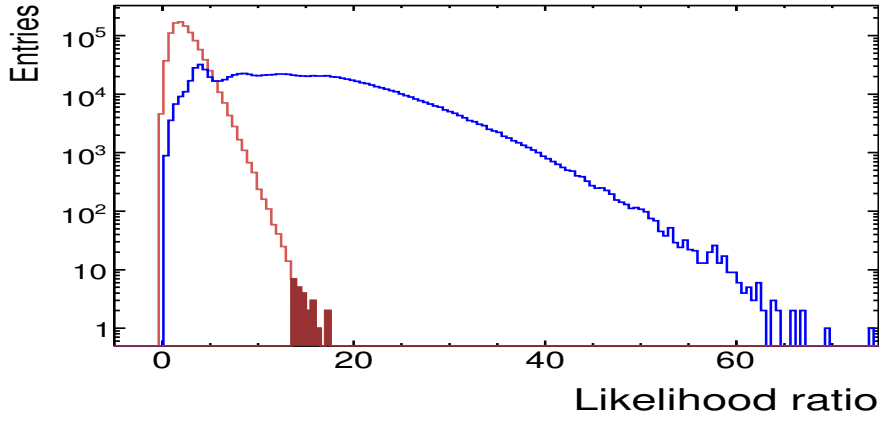


Figure 48: Likelihood ratio distribution for a 3 TeV $Z'_{SSM} \rightarrow ee$; the distribution on the left (in red) corresponds to background-only pseudoexperiments; the one on the right (in blue), to signal plus background.

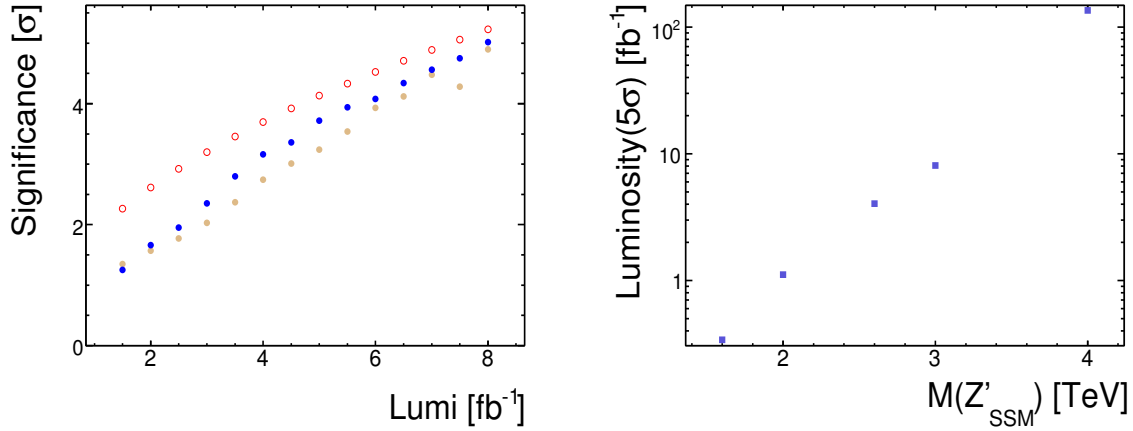


Figure 49: Left: Comparison of the significance obtained from the number-counting approach (red hollow circles), a fixed-mass fit with a variable signal cross section (blue dots), and a fit-based approach where the mass is a free parameter. Right: Luminosity needed for a 5 sigma significance using a fit-based approach

expected significance as:

$$\mathcal{S} = \sqrt{2 \left((s+b) \ln \left(1 + \frac{s}{b} \right) - s \right)} \quad (19)$$

Figure 49.left shows a comparison between the expected significance for a 3 TeV SSM Z' , as obtained from pure Number Counting in red circles, a fit in which the signal mass is fixed to the correct value, but the normalization is free to float (blue dots), and a fit in which both the location and the normalization of the dilepton resonance float. Figure 49.right show the necessary luminosity for a 5σ discovery for different Z'_{SSM} masses.

Full simulation analysis The efficiency for selecting two electrons coming from a Z' has been studied in samples of fully simulated events. It depends on the coupling of the Z' to the fermions, via the different rapidity distributions generated by the different Parton Density Functions (PDF) of the incoming quarks. Indeed, the PDF of the up quarks being harder than that of the down quarks, Z' produced by a $u\bar{u}$ pair tend to be slightly more boosted, and therefore the electrons stemming from their decay tend to be produced

at slightly higher pseudo-rapidities. However, if one separates the electron pairs coming from $u\bar{u}$ and $d\bar{d}$ pairs, the dielectron rapidity distribution is independent of the model, and so is the electron/positron pseudo-rapidity distribution, as shown in [53].

The selection which is most sensitive to the η distribution of the electron/positron is obviously the requirement that its absolute value be less than 2.5, which is the first criteria for a cluster to be called a *reconstructed* electron (see section 3.1). One can see its efficiency on Figure 50 (left) as a function of the generated dielectron mass for $u\bar{u}$ and $d\bar{d}$ pairs separately (at the generated level). The $u\bar{u}$ efficiency is about 10% lower than the $d\bar{d}$ efficiency at 500 GeV, and this difference tends to decrease as the invariant mass increases, as expected since the pseudo-rapidity of the electron/positron is more and more narrow. The next selection is the matching of candidate clusters with tracks, which results in a sample of *reconstructed* electrons.

In selecting electron pairs, the simplest requirement after demanding two *reconstructed* electrons is that they be both identified as *loose* electrons. The relative efficiency of such a selection is at least 94% and slightly increases with the invariant mass. The next selection which can be applied is the requirement of two opposite electric charges. The combined relative efficiency remains above 90%. Although this requirement is optional in the absence of a large background, especially at very high invariant mass, it allows to have a control sample (made of same sign dielectrons) for the background.

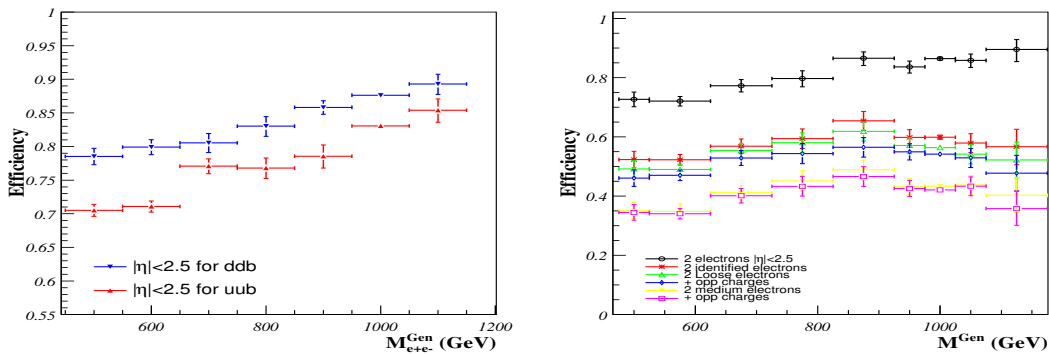


Figure 50: Dielectron selection efficiency as a function of the generated invariant mass. Left: $|\eta| < 2.5$ criteria for $u\bar{u}$ and $d\bar{d}$ events separately; right: 2 reconstructed electrons, *loose*, *medium* and opposite charge selections.

We have checked the requirement of two *medium* electrons and found that its relative efficiency (with respect to two reconstructed electrons, not with respect to two *loose* electrons) was between 72% and 76% without the requirement of opposite electric charges, and between 70% and 74% with the opposite charge requirement.

The efficiency of all these criteria applied sequentially is shown as a function of the invariant mass of the dielectron pair on Figure 50 (right) for the example case of the $E_6 \chi$ model with $M(Z')=1 \text{ TeV}^3$. In this model, the proportion of $u\bar{u}$ pairs in the initial state is relatively low (about 20%) and therefore the efficiency is relatively high (close to the $d\bar{d}$ efficiency) around the peak. An opposite example is given by the Drell-Yan, which has an inverse fraction of $u\bar{u}$ pairs in the initial state and whose efficiency is thus relatively low (close to the $u\bar{u}$ value). Therefore, even in a sample of simulated dielectrons with a Z'_χ contribution, the efficiency is lower at low masses, where only the Drell-Yan contributes, than at the Z'_χ peak. The resulting total efficiency for masses between 500 and 1200 GeV is between 45 and 55% with a *loose* electron plus opposite charge selection, and between 35 and 45% with a *medium* electron plus opposite charge selection in the fully simulated Z'_χ sample.

³⁾Fully simulated dataset number 5605

6.3 $G^* \rightarrow e^+e^-$ in a non-parameterised approach

In this channel, we assume that there is no interference between the G^* and the dilepton background. This allows us to use the non parameterised CLs method [51]. In table 14, we show Monte Carlo parameters of the used G^* . Γ_G is the simulated graviton resonance width, and Γ_m stands for the width of observed resonance after convolution with detector resolutions. In this model, the graviton with $k/\bar{M}_{pl} < 0.06$ has a true width much smaller than the experimental resolution. The Graviton to e^+e^- channel is a very clean channel. The main Standard Model background is Drell-Yan dielectron production. Other backgrounds such as dijets with both jets misidentified as electrons are neglected at this moment.

$G^* (M k/\bar{M}_{pl})$	Γ_G [GeV]	Γ_m [GeV]	$\sigma \cdot BR(G^* \rightarrow e^+e^-)$ [fb]	DY $\sigma \cdot BR(\rightarrow e^+e^-)$ [fb]
750 GeV 0.01	0.05	7.0	27.7	33.7
1.0 TeV 0.02	0.28	8.0	26.0	12.5
1.2 TeV 0.03	0.83	10.7	22.4	4.7
1.3 TeV 0.04	1.2	12.3	25.3	3.0
1.4 TeV 0.05	2.1	13.0	26.8	2.0

Table 14: Parameters of the used $G^* \rightarrow ee$ samples and Drell-Yan cross section in a window of 300 to 400 GeV under the peak.

Resonance selection In reconstructing the resonance mass, we require a pair of *loose* electrons⁴⁾, as described in section 3.1, with opposite charge. Since the spin of the Graviton is different from the spin of the Z' , the η distribution of the electrons and positrons stemming from Graviton and Z' are different and therefore the efficiency for selecting dielectron pairs is different. On average, the selection efficiency for Graviton events is 58% with respect to the number of generated events.

From table 15, for instance, the *loose* selection gives an efficiency of $55.9 \pm 1.2\%$ for Graviton of $M=1.2\text{TeV}$, $k/\bar{M}_{pl}=0.03$. Note that the efficiency decreases with graviton mass, which is consistent with the study of section 3.1.

Selection	750 GeV 0.01	1.0 TeV 0.02	1.2 TeV 0.03	1.3 TeV 0.04	1.4 TeV 0.05
<i>Loose</i> Eff	$65.5 \pm 1.1\%$	$62.0 \pm 1.0\%$	$55.9 \pm 1.2\%$	$55.6 \pm 1.1\%$	$52.6 \pm 1.1\%$

Table 15: *Loose* selection efficiency, calculated from 2000 MC events.

For Drell-Yan e^+e^- background, a fitting function $\exp(-2.2M^{0.3})$ is shown to be a good approximation to extrapolate the background shape to the higher invariant mass region.

Discovery Potential Using the non parameterised CLs method, pseudo experiments are generated from null hypothesis, H0 (DY background) and test hypothesis, H1 (DY with G^* resonance) and the distribution of logarithm of the likelihood ratio are constructed. Contrast to real experiment where we can compare the Standard Model with experimental data directly, in planned experiment 5σ discovery limits

⁴⁾isEM & 0x7 = 0

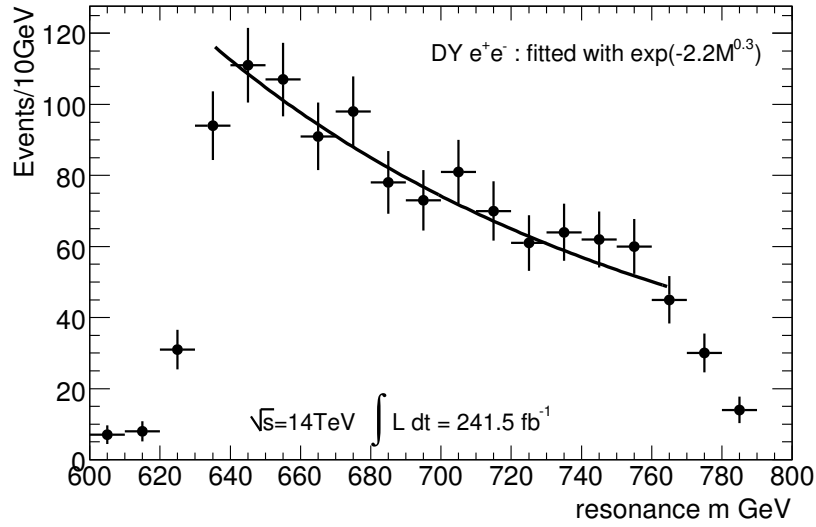


Figure 51: Drell-Yan: distribution of invariant mass of two reconstructed electrons

and 3σ evidence limits are calculated assuming new physics exists, the 95% exclusion limit is obtained with the assumption of null hypothesis. Figures 52 and 53 show, respectively, the 5σ discovery, 3σ evidence limits and the 95% exclusion limits estimated for an integrated luminosity of 1 fb^{-1} and for different values of the k/M_{pl} parameter. For the limit setting, the LO cross sections and k-factor for both signal and DY background are used. Next-to-leading-order (NLO) calculations have shown that SM has an expected k-factor of ≈ 1.26 , while Graviton has k-factor of ≈ 1.6 , both of them are more or less flat in the region concerned [54]. Various sources of systematic uncertainties for signal and background are considered in the evaluation of the experimental sensitivity as in section 5.1.3.

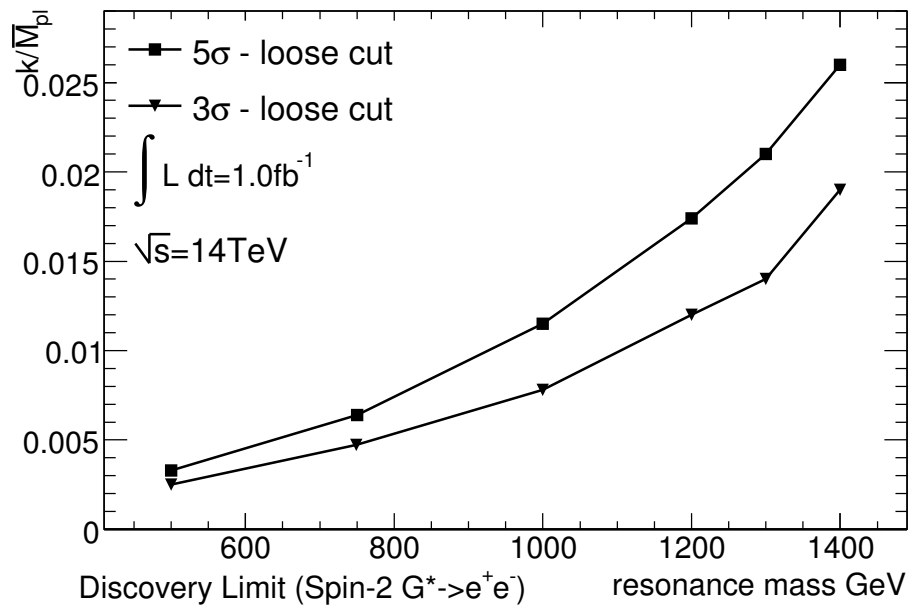
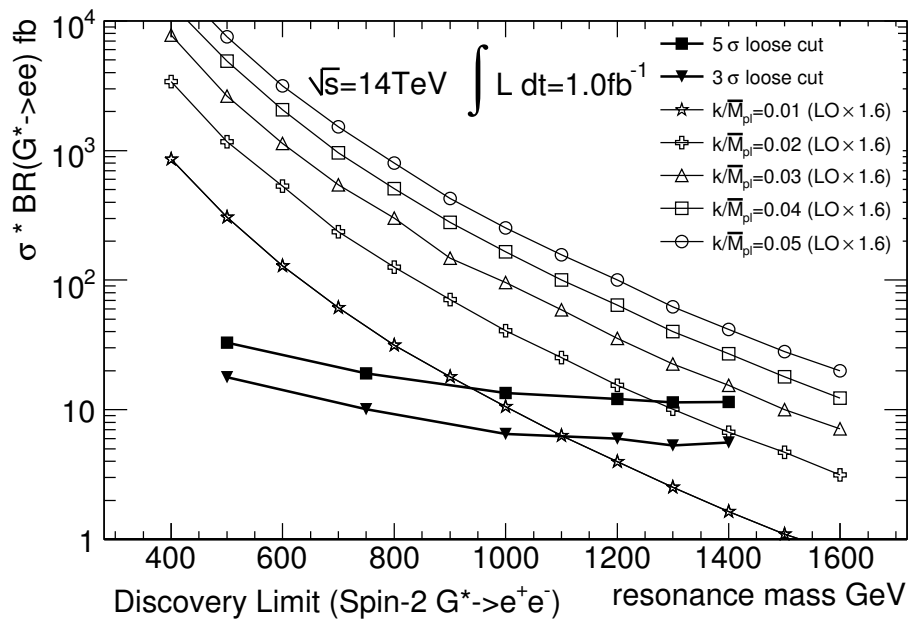


Figure 52: 5 σ discovery (full square) and 3 σ evidence (full triangle down) limits. The other lines with open marks are cross-section for several couplings generated by PYTHIA.

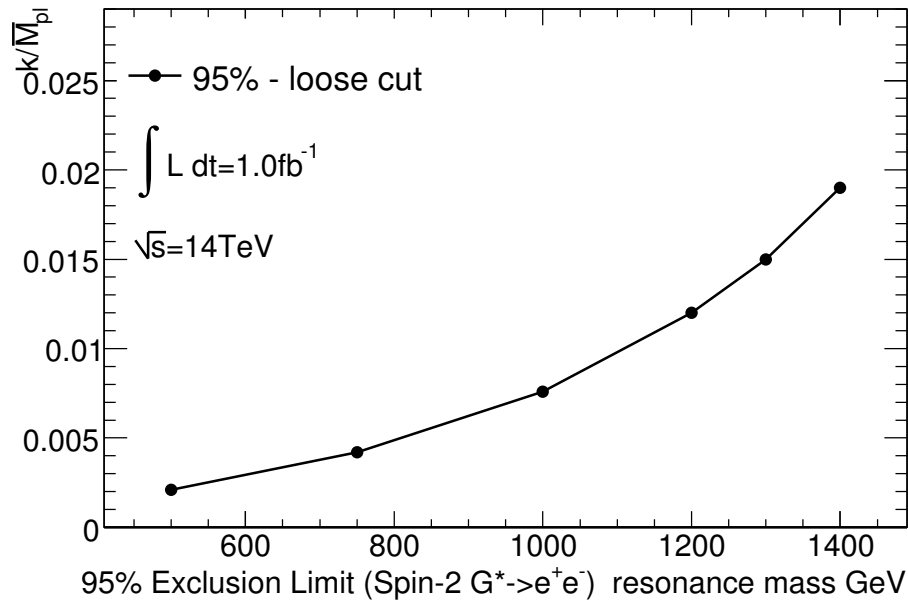
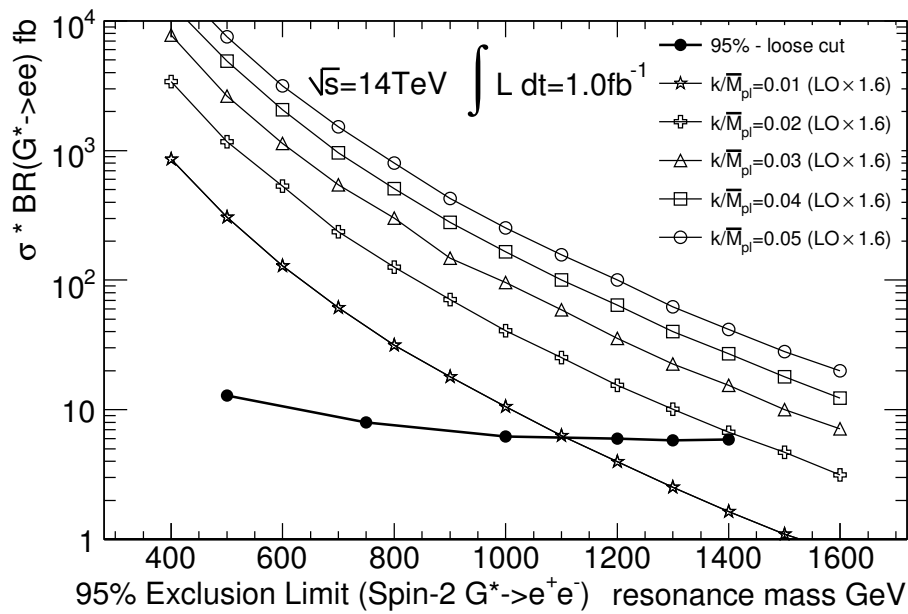


Figure 53: 95% exclusion (full circle) limits. The other lines with open marks are cross-section for several couplings generated by PYTHIA.

6.4 $G \rightarrow \tau\tau$ using the number counting approach

Ditau Background Evaluation From previous experiments we know that there are many effects which are not very well modelled by Monte Carlo generators. Due to the enormous cross-sections of various background processes, all low probability effects start playing an important role. An effort is now being made to develop techniques which will enable one to measure the τ misidentification rate from real data when LHC collisions begin. Another issue is that due to the enormous rejection factor required against QCD dijets we do not have enough statistics to study the full event selection using Monte Carlo samples. As a first approximation we can treat the probability of having an identified tau as being uncorrelated with other selection criteria.

It should be noted that i) the probability of having an identified lepton increases with the P_T of the hard process of the jet, ii) the misidentification of hadronic taus is E_T dependent, iii) the QCD jet cross section decreases with P_T of the hard process.

The event selection for the lepton-hadron final-state is as follows:

(a) **Trigger**

For this iteration of the analysis, and with the 12.0.6.X series of the ATLAS software, we only consider lepton triggers. We are using `Trig_EF_e25i`, `Trig_EF_e60`, and `Trig_EF_mu20i`. We require that at least one of these triggers be fired and an event is not rejected if more than one was fired.

(b) **Lepton Selection**

We require a track-match and impose the *medium* electron selection by requiring logical AND of 0x3FF with the `IsEM` bit to be zero. Note that the electron selection in this analysis was tightened from that used elsewhere in this note as the default selection reduced the overall significance by roughly a factor of two.

The isolation requirement imposed on electron candidates is $\sum_i ET_{EM<0.2}/P_T < 0.1$ where $\sum_i ET_{EM<0.2}$ is the sum of the energy deposits in the electromagnetic calorimeter within a cone of $\Delta R = 0.2$ from the location in η - ϕ of the electron, less the electron candidate energy. Isolated electrons are required to have $|\eta| < 2.5$ and $P_T > 25$ GeV/c.

We impose an isolation requirement similar to that of electrons on muon candidates: $\sum_i ET_{EM<0.2}/P_T < 0.1$ where $\sum_i ET_{EM<0.2}$ is the sum of the energy deposits in the electromagnetic calorimeter within a cone of $\Delta R = 0.2$ from the location of the muon candidate in η - ϕ . For isolated muons we require that the χ^2 lie between 0 and 20 and to be considered by the analysis muons must have $|\eta| < 2.5$ and $P_T > 20$ GeV/c.

(c) **Hadronic Tau Selection**

We consider hadronic tau from `tauRec` block and impose a requirement on the log-likelihood (`llh`) as a function of the tau E_T as outlined in Section 3.4. Tau candidates which overlap ($\Delta R < 0.2$) with tight electrons and muons are removed. We require the hadronic tau $p_T > 60$ GeV/c.

(d) **Opposite Charge**

We require that the product of the hadronic tau and lepton charges be ≤ 0 .

(e) **Missing Transverse Energy**

The Object-Based missing transverse energy is used in this analysis and we impose the requirement that the MET > 30 .

(f) **Total Event P_T**

To greatly help with the rejection of the `t` $\bar{t} backgrounds we employ a cut on the total event $P_T$$

which is defined as the sum of the MET and the vector sum of the hadronic tau with the lepton transverse momentum. We require $P_{T,tot} < 70$.

(g) **Transverse Mass**

The transverse mass of the event is determined by using the lepton and the event MET. The M_T is cacluated as:

$$M_T = \sqrt{2 \cdot P_{T,l} \cdot P_{MET} (1 - \cos \Delta\phi_{l,MET})}$$

We require that $M_T < 50 \text{ GeV}/c^2$

(h) **Visible Mass**

A visible mass variable is calculated as defined by CDF [55] using the tau and lepton four-vector information in addition to building a four-vector for the missing energy:

$$\vec{p}_{MET} = (MET_x, MET_y, 0, |MET|)$$

and to greatly help with background rejection we require $M_{vis} > 300 \text{ GeV}$.

(i) **Invariant Mass Reconstruction**

The collinear approximation is used to build up the event-by-event invariant mass. The fraction of the tau momentum carried by the visible decay daughters, x_{lep} and x_{had} , are cacluated with the following formulas:

$$x_{lep} = \frac{p_{x,lep} p_{y,had} - p_{x,had} p_{y,lep}}{p_{y,had} p_{x,lep} + p_{y,had} \cancel{p}_x - p_{x,had} p_{y,lep} - p_{x,had} \cancel{p}_y}$$

$$x_{had} = \frac{p_{x,lep} p_{y,had} - p_{x,had} p_{y,lep}}{p_{y,had} p_{x,lep} + p_{x,lep} \cancel{p}_y - p_{x,had} p_{y,lep} - p_{y,lep} \cancel{p}_x}$$

The collinear approximation breaks down when the two taus are back-to-back, so we impose the requirement that $\cos \Delta\phi_{lh} > -.99$. The reconstructed mass is then calculated as:

$$M_{\tau\tau} = \frac{M_{lh}}{\sqrt{x_{lep} x_{had}}}$$

where we require $0 < x_{lep} < 0.75$ and $0 < x_{had} < 1.0$.

Ditau Systematic Uncertainties: The uncertainties considered are those described in section 5.1.3.

Significance in 1 fb^{-1} of data: Table 16 shows the cross section remaining, in pb, for the signal as well as all background processes considered. Here we assume a $600 \text{ GeV}/c^2$ $Z\tau$ and the SSM cross section. In 1 fb^{-1} of ATLAS data we estimate 153.2 signal events and 390.1 background events after imposing the event selection up to the cut on visible mass (Cuts (a) - (h)). Using S/\sqrt{B} we estimate the signal significance to be 7.76.

Distributions of the visible and reconstructed masses for signal and background are shown here:

Cut	signal σ [pb]	Z+jets σ [pb]	ttbar σ [pb]	QCD σ [pb]	W+jets σ [pb]
	3.639	1.86e+03	461	9.95e+07	2.83e+04
(a) Trigger	1.36	1.33e+03	219	1.22e+03	525
(b) Lepton	0.928	578	162	329	354
(c) Tau selection	0.411	44.7	8.57	268	77.6
(d) Opposite Charge	0.359	28.1	3.04	189	26.5
(e) MET > 30	0.309	0.77	2.52	28.8	14.8
(f) MT < 50	0.238	0.502	0.592	24.8	1.57
(g) pT TOT < 70	0.177	0.237	0.192	24	1.22
(h) Mvis > 300	0.153	0.0152	0.0621	0.206	0.106
(i) Tau Reco	0.0176	0	0.0082	0.022	0.00776

Table 16: Cutflow table for the $Z' \rightarrow \tau\tau \rightarrow lh$ analysis with *medium* electron selection. The significance in 1 fb^{-1} of data is 7.76. Here we consider a $600 \text{ GeV}/c^2$ Z' and the SSM cross-section.

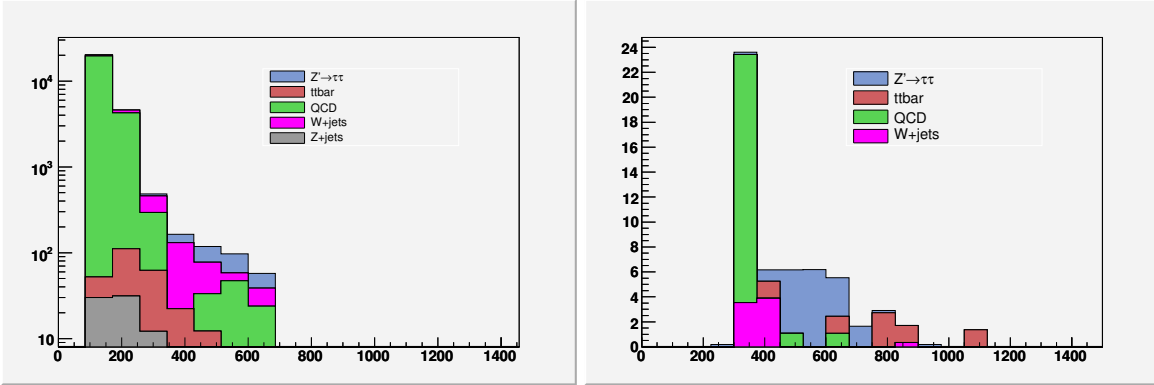


Figure 54: Left: The visible mass distribution in the $Z' \rightarrow \tau\tau \rightarrow lh$ analysis for signal and background processes (1 fb^{-1} of data is assumed). Right: The reconstructed invariant mass obtained using the collinear approximation.

6.5 $G \rightarrow \gamma\gamma$ using number counting approach

The diphoton signature provides an important search strategy for graviton in the Randall-Sundrum model [8]. The excellent energy resolution of the calorimeter provides a narrow invariant mass distribution. However, significant background diphoton production occurs within any mass window from QCD direct photon processes. Other backgrounds are instrumental: single γ + jets, and QCD multijet production.

An analysis searching for $G \rightarrow \gamma\gamma$ must accomplish several goals. The expectation for the kinematics of background processes must be established, and uncertainties from *pdfs* and other effects must be estimated. This will allow an accurate background model and therefore a useful estimate of the mass-dependence of the search. Removal of instrumental backgrounds necessitates determination of photon performance at much higher energies than is typical for most ATLAS analyses. The particulars of signal and background levels in this mass range may motivate a somewhat changed photon identification to improve sensitivity, and reduce systematics. We will discuss our studies of these issues in the following sections.

We describe here an estimate of the $G \rightarrow \gamma\gamma$ event yield. Once the photon identification has been optimized, it remains to understand any remaining dependence of efficiency for gravitons of different mass. We provide event yield estimates for two different mass points: 500 GeV and 1 TeV.

Estimation of efficiency Our basic preselection for Graviton events is two photons with isolation and medium identification cuts, and $p_T > 20$ GeV each. With these cuts, we have determined the dependence of the selection vs. $M_{\gamma\gamma}$ when both photons are in the barrel, one is in the endcaps, or both are in endcaps. These distributions are shown in figure 55.

Background The backgrounds to the $G \rightarrow \gamma\gamma$ signal involve both instrumental effects ('fake photons') and the normal QCD production of two isolated, direct photons:

- Diphoton continuum: The QCD diphoton process was simulated using PYTHIA with two photons having $p_T > 100$ GeV. Tables 18 and 17 show the event yields in the mass window around the Graviton production mass.
- Instrumental background: we expect to estimate the instrumental background based on a fake-rate folded into the yield of events with one tight photon and one loose or raw photon. We have studied the kinematic distribution in the single photon plus jet, and multijet samples by using a 'raw-tight' selection.

The invariant mass distributions including all the backgrounds is given in figure 55.

Event Yields Tables 17 and 18 provide an itemization of the number of events generated, theoretical cross sections, total event yields in mass window, and total number of events in mass window when scaled and 1 fb^{-1} . Figure 55 shows a stacked histogram of the invariant mass distribution from various samples. These samples all use only the baseline photon id cuts and no isolation with exception to the DiJet J6 sample. For this sample no photon id cuts were applied in order to get a statistically significant distribution. This distribution was then scaled by the photon id cut efficiency.

Sensitivity to $G \rightarrow \gamma\gamma$ From our estimated signal and background yields, we have calculated the significance of the diphoton excess from Gravitons. We use the expression $S = 2(\sqrt{s+b} - \sqrt{b})$ to define significance. Table 19 indicates the value of S calculated for the 500 GeV and 1 TeV Gravitons in 1 fb^{-1} and 10 fb^{-1} of collider data. From this definition, we scan to determine how much luminosity we need to obtain a 3σ or 5σ excess for each of the two mass points we consider. Figure 6.5 indicates the luminosity projection vs. Graviton mass for these levels of significance.

Table 17: Number of events generated, cross section(CS), and yields in $448 < m_{\gamma\gamma} < 544$ GeV before scaling and scaling to 1fb^{-1}

Sample	N	CS	Yield $448 < m_{\gamma\gamma} < 544$	Yield $448 < m_{\gamma\gamma} < 544$ GeV; 1fb^{-1}
Graviton (500 GeV)	10000	0.052	5827	30
Diphoton	1789	0.66	58	21
$\gamma + Jet$	9000	11.8	6	8
Dijet J5	389350	12500	1752	8
Dijet J6	381450	360	0	0

Table 18: Number of events generated, cross section (CS), and yields in $950 < m_{\gamma\gamma} < 1050$ before scaling and scaling to 1fb^{-1}

Sample	N	CS	Yield $950 < m_{\gamma\gamma} < 1050$	Yield $950 < m_{\gamma\gamma} < 1050$; 1fb^{-1}
Graviton (1 TeV)	1500	0.0147	758	7
Diphoton	1789	0.66	6	2
$\gamma + Jet$	9000	11.8	0	0
Dijet J5	389350	12500	125	0
Dijet J6	381450	360	0	0

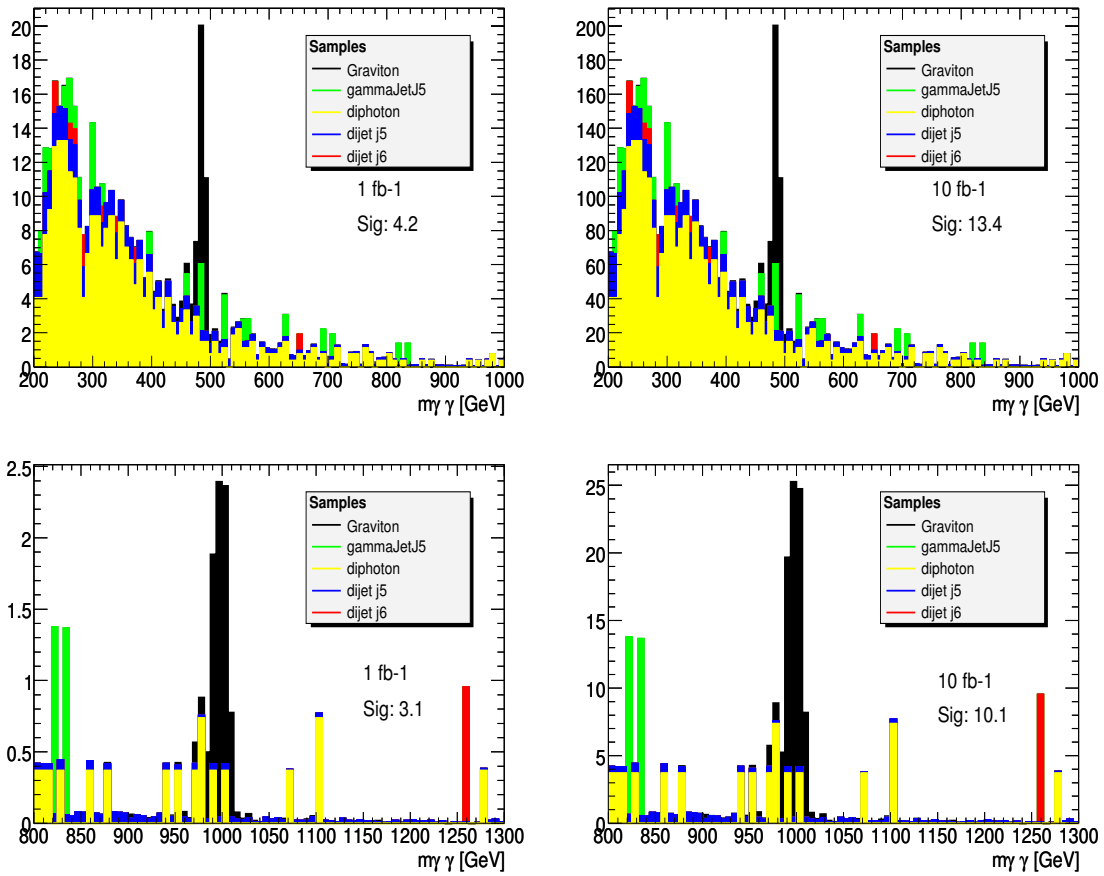


Figure 55: $m_{\gamma\gamma}$ Invariant mass: (upper) for 500 GeV Graviton in 1fb^{-1} and 10fb^{-1} . (lower) for 1 TeV Graviton in 1fb^{-1} and 10fb^{-1} .

Table 19: Signal significance at 1 and 10 fb^{-1} for 500 GeV and 1 TeV Graviton samples.

Sample	CS	Significance 1fb^{-1}	Significance 10fb^{-1}
Graviton (500 GeV)	0.052	4.2	13.4
Graviton (1 TeV)	0.0147	3.1	10.1

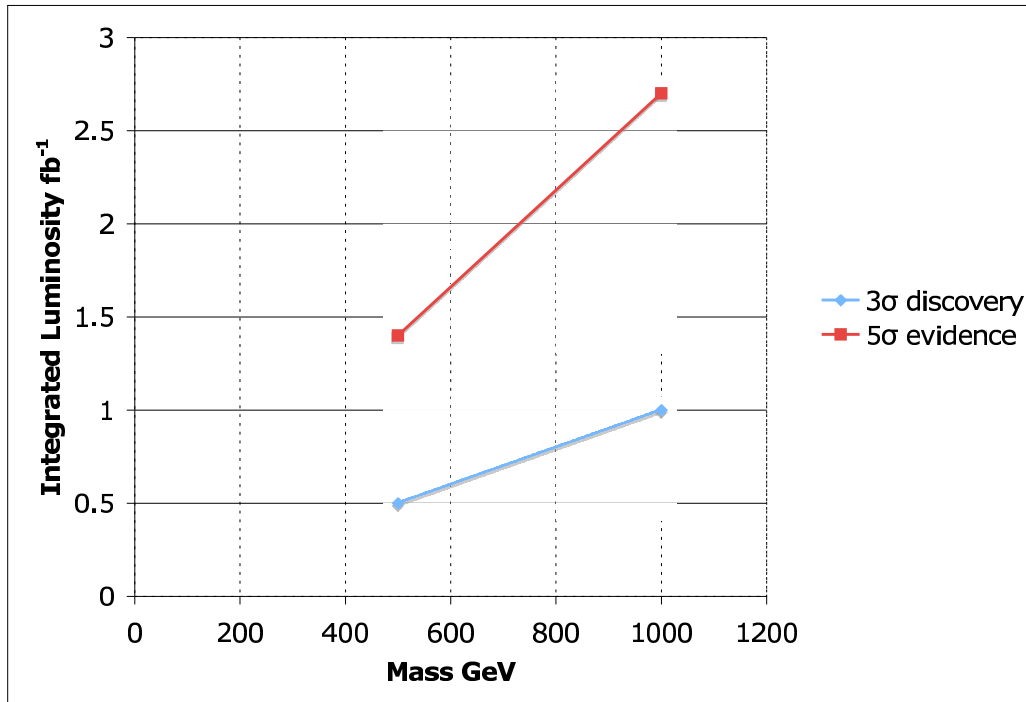


Figure 56: Required luminosity to obtain 3 σ and 5 σ excesses for Gravitons of mass 500 GeV and 1 TeV.

6.6 Technicolor using a non parameterised approach

Topcolor-assisted Technicolor models with walking gauge coupling predict new technihadron states that are copiously produced at the LHC. The lowest mass states are the scalar technipions ($\pi_T^{\pm,0}$) and the vector technirho and techniomgega ($\rho_T^{\pm,0}$ and ω_T^0). The vector mesons decay into a gauge boson plus technipion ($\gamma\pi_T$, $W\pi_T$ or $Z\pi_T$) and fermion-antifermion pairs. This analysis searches for the decays $\rho_T \rightarrow \mu^+\mu^-$ and $\omega_T \rightarrow \mu^+\mu^-$. The dimuon mode has a lower branching fraction than the modes involving technipions but the signal is clean, straightforward to trigger on, and can be readily observed with early ATLAS data.

The particular model studied here is the ‘‘Technicolor Strawman Model’’ or TCSM [56, 57]. In the TCSM, it is expected that techni-isospin is an approximate good symmetry and therefore the isotriplet ρ_T and isosinglet ω_T will be nearly degenerate. We will assume for what follows that $M(\rho_T) = M(\omega_T)$. The technipions are also expected to be nearly degenerate. In the TCSM, the technipion masses are generically not small. In particular, $M(\pi_T) > M(\rho_T)/2$ and therefore the decays of the ρ_T and ω_T to technipions is kinematically forbidden. The dimuon rate is expected to come dominantly from the ω_T with a smaller contribution from the ρ_T .

We use STACO muons that are the best match to an inner detector track. The event selection is summarized in Table 20.

Table 20: Cut flow for the analysis. Errors are statistical only.

$M(\rho_T, \omega_T)$ (GeV)	400	600	800	1000
Peak Mass (GeV)	403	603	804	1004
$\sigma(M)$ (GeV)	13	22	34	46
Cut Flow				
Generated	10000	10000	9500	10000
$ \eta < 2.5$	5772	6557	6556	7184
$p_T > 30$ GeV	5691	6494	6492	7129
L1_MU20 L1_MU40	5566	6365	6334	6952
L2_mu20i	5492	6260	6248	6861
EF_mu20i	5438	6168	6156	6759
Opposite charge	5431	6161	6125	6729
Mass Window	4003	4429	4391	4826
Selection Efficiency (%)	40.0 ± 0.5	44.3 ± 0.5	46.2 ± 0.5	48.3 ± 0.5

In principle, the best search sensitivity is not obtained by examining the entire dimuon mass distribution for a bump all at once but by using an optimized mass window that maximizes the signal significance for a given assumed signal mass. A prescription for the optimal window size was by an analytic calculation in Ref. [58]. Assuming a narrow Gaussian peak on a linear background, the optimal window was found to be $\pm 1.4\sigma$ about the peak mass. Since we are not really in the narrow resonance regime, we did a study using full-simulation ATLAS Monte Carlo for a Technicolor signal on a Drell-Yan background. Taking S/\sqrt{B} as our measure of significance, figure 57 shows that a window size of $\pm \sim 1.5\sigma$ or a bit larger is optimal. For this study, we use a window size of $\pm 1.5\sigma$ about the peak mass.

A proper study of the systematic uncertainties for this analysis has not been performed yet. In lieu of that study, we take representative uncertainties from earlier new particle searches in the dimuon channel, either at the Tevatron or LHC. The uncertainties considered are those described in section 5.1.3.

Cross section limits were calculated under two integrated-luminosity scenarios, 100 pb^{-1} and 1

Figure 57: For two different ρ_T, ω_T signal masses, S/\sqrt{B} is plotted as a function of mass-window size for windows centered on the peak mass.

Figure 58: The green curve is Technicolor $\sigma \times B$ as a function of ρ_T, ω_T mass. The red (dotted) curves correspond to 95% CL limits based on integrated luminosity of 100 pb^{-1} , the blue (solid) curves are for 1 fb^{-1} . Curves labeled “Bayesian” used the DØ Bayesian limit calculator for events in the optimized mass window. Curves labeled “CLs” use limits from the mclimit program for events in the optimized mass window.

Figure 59: Integrated luminosity needed for 3σ evidence or 5σ discovery as a function of ρ_T, ω_T mass.

A Effect of alignment On the sensitivity to $Z' \rightarrow \mu\mu$ channel

In order to quantify the impact of the misalignment on the dimuon channel we performed a significance analysis. The goal of this significance analysis is to put limits on the Z' discovery potential as a function of misalignment. This is a preliminary analysis, the systematic effect are not include. The method we use is a Likelihood Ratio based on a non-parameterised approach, with the hypotheses H0 and H1. We performed a lot of pseudo experiment for background and signal-plus-background for each alignment configuration. For this, we use a Poisson distribution. We did the calculation of H0 and H1 which are defined as follow:

$$L_0 = \prod_{bins_i} P_0(\lambda_i, k_i) \quad L_1 = \prod_{bins_i} P_1(\lambda_i, k_i) \quad \text{with} \quad P(\lambda_i, k_i) = \frac{\lambda_i^{k_i} \cdot e^{-\lambda_i}}{k_i!}$$

We define the Likelihood ratio as

$$-2 \cdot \ln(Q) = -2 \cdot \ln\left(\frac{L_1}{L_0}\right)$$

and we define the significance as the calculation of the integral of the signal-plus-background (in blue) curve after the median of the background curve (in red), see Fig. 60

The results of the significance calculation for different luminosity and alignment scenario is shown on figure 61. The horizontal black line correspond to an exclusion limit at 3σ . So we need 10.5 pb^{-1} to exclude a 1 TeV at 3σ Z' with the nominal alignment, and 16.5 pb^{-1} for the 1mm alignment scenario. The shape of the yellow curve *ie* for the 200 μ m hypothesis is due to a lack of statistic.

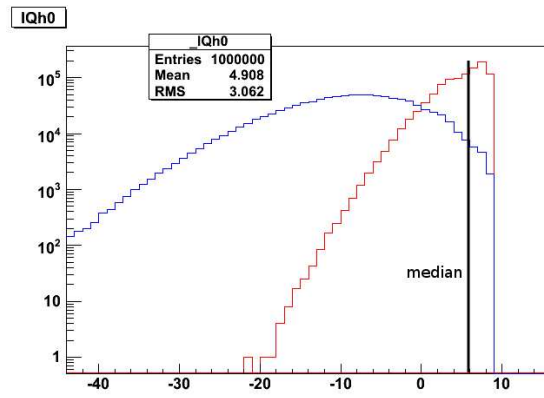


Figure 60: Q distribution for 1mm misalignment hypothesis. In blue signal+background, in red background

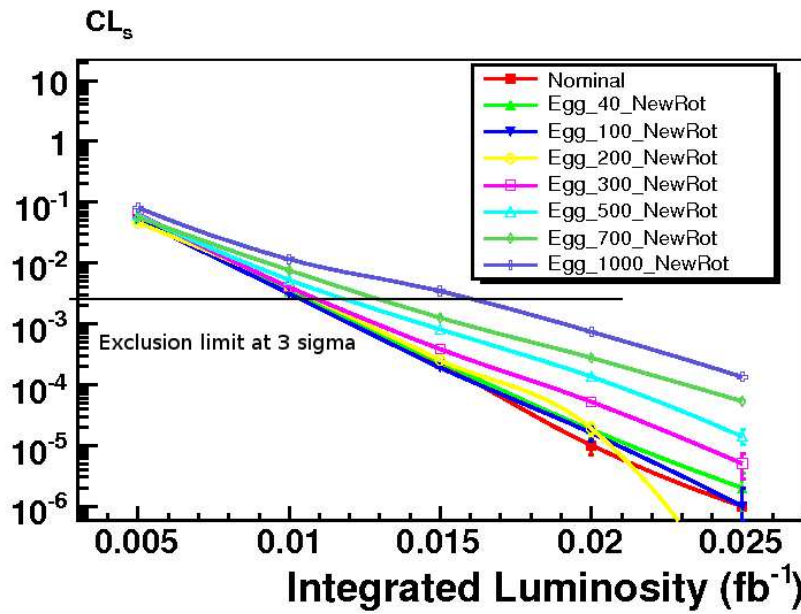


Figure 61: Exclusion limit at 3σ as a function of luminosity for different misalignment configuration.

References

- [1] J.J. Aubert *et al.* Experimental observation of heavy J/ψ . *Phys. Rev. Lett.*, 33, 1974.
- [2] J.E. Augustin *et al.* Discovery of a narrow resonance in e^+e^- annihilation. *Phys. Rev. Lett.*, 33, 1974.
- [3] J.P. Appel *et al.* Observation of a dimuon resonance at 9.5 gev in 400 gev proton -nucleon collisions. *Phys. Rev. Lett.*, 39, 1977.
- [4] G. Arrignon *et al.* Experimental observation of lepton pairs of invariant mass around $95 \frac{GeV}{c^2}$ at the cern sps collider. *Phys. Lett.*, 126, 1983.
- [5] H. Georgi and S.L. Glashow. *Phys. Rev. Lett.*, 32, 1974.
- [6] K. Lane and E. Eichten. *Phys. Lett. B*, 222, 1989.
- [7] N. Arkani-Hamed A.G.Cohen and H.Georgi. *Phys Letters B*, 513, 2001.
- [8] L. Randall and R.Sundrum. *Phys. Rev. Lett.*, 83, 1999.
- [9] [D0 Collaboration]. Search for randall-sundrum gravitons in dilepton and diphoton final state. *Phys. Rev. Lett.*, 95, 8 2005.
- [10] A. Abulencia *et al.* [CDF Collaboration]. Search for $Z' \rightarrow e^+ e^-$ using dielectron mass and angular distribution. *Phys. Rev Lett.*, 96, 6 2006.
- [11] The LEP Collaborations ALEPH DELPHI L3 OPAL and the LEP Electroweak Working Group. A combination of preliminary electroweak measurements and constraints on the standard model. *arXiv:hep-ex*, 0511027, 2005.
- [12] G. Abbiendi *et al.* [OPAL Collaboration]. *Eur. Phys. J. C*, 33, 2004.
- [13] G. Abbiendi *et al.* [OPAL Collaboration]. *Eur. Phys. J. C*, 6, 1999.
- [14] G. Abbiendi *et al.* [OPAL Collaboration]. *Eur. Phys. J. C*, 2, 1998.
- [15] J. Abdallah *et al.* [DELPHI Collaboration]. *Eur. Phys. J. C*, 45, 1999.
- [16] P5 Comittee. The case for run ii: Submission to the particle physics project prioritization panel the cdf and d0 experiments. 2005.
- [17] The ATLAS Collaboration. $Z' \rightarrow e^+e^-$ studies in full simulation (dc1). ATL-PHYS-PUB-2005-010, 2005.
- [18] Benjamin Trocme for the ATLAS Collaboration. Searching for Z' and model descrimination in atlas, 2005.
- [19] The ATLAS Collaboration. Z' at the lhc. ATL-PHYS-PUB-2006-024, 2006.
- [20] The ATLAS Collaboration. Atlas monte carlo - the inside story, behind the numerical integration. ATLAS-NOTE-XXX, 2007.
- [21] The ATLAS Collaboration. find a reference for athena. ATLAS-NOTE-XXX, 2007.

- [22] Peter Skands Torbjorn Sjostrand, Stephen Mrenna. Pythia 6.4: Physics and manual. hep-ph/0603175, 2006.
- [23] The ATLAS Collaboration. E/gamma reconstruction and identification. ATLAS-NOTE-YYY, 2007.
- [24] The ATLAS Collaboration. The atlas experiment at the cern large hadron collider. 2008.
- [25] The ATLAS Collaboration. The atlas muon spectrometer technical design report, 1997.
- [26] The ATLAS Collaboration. Muon reconstruction and all that jazz, 2007.
- [27] W.-M. Yao *et al.* Review of particle physics. *Journal of Physics*, G33:12322, 2006.
- [28] ATLAS Collaboration. Muons in calorimeters: energy loss corrections and muon tagging. 2007.
- [29] D. Cavalli M. Heldmann. An improved τ -identification for the atlas experiment. ATLAS-PHYS-PUB-2006-008, 2006.
- [30] T. Ahmed *et al.* H1 Collab. Energy flow and charged particle spectra in deep inelastic scattering at hera. *Z. Phys.*, C63:377, 1994.
- [31] The ATLAS Collaboration. Strawman trigger menu, 2007.
- [32] Overview of the electron trigger algorithms, available from the atlas twiki: <https://twiki.cern.ch/twiki/bin/view/atlas/trigelectronoverview>.
- [33] Overview of the photon trigger algorithms, available from the atlas twiki: <https://twiki.cern.ch/twiki/bin/view/atlas/trighltphtonhypo>.
- [34] e/gamma Group. Eg csc note. 2007.
- [35] Normalizations to be used in e/gamma studies, available from the atlas twiki: <https://twiki.cern.ch/twiki/bin/view/atlas/trigegammanormalise>.
- [36] E/ γ trigger menu for $\mathcal{L}=10^{31}$, available from the atlas twiki: <https://twiki.cern.ch/twiki/pub/atlas/l31triggermenu/l31egammamenu.pdf>.
- [37] W.-M. Yao *et al.* Review of Particle Physics. *Journal of Physics G*, 33:1+, 2006.
- [38] J. Pumplin, D. R. Stump, J. Huston, H. L. Lai, P. Nadolsky, and W. K. Tung. New generation of parton distributions with uncertainties from global qcd analysis. *JHEP*, 0207:012, 2002.
- [39] A. D. Martin, W. J. Stirling, and R. S. Thorne. Mrst partons generated in a fixed-flavour scheme. *Physics Letters B*, 636:259, 2006.
- [40] ZEUS Collaboration. An nlo qcd analysis of inclusive cross-section and jet-production data from the zeus experiment. *European Physical Journal C*, 42:1, 2005.
- [41] G. Corcella, IG Knowles, G. Marchesini, S. Moretti, K. Odagiri, P. Richardson, MH Seymour, and BR Webber. Herwig 6.5 release note, 2002.
- [42] M. Seymour J. Butterworth, J. Forshaw and R. Walker. Jimmy generator, multiparton interactions in herwig.
- [43] Daniel Stump, Joey Huston, Jon Pumplin, Wu-Ki Tung, H. L. Lai, Steve Kuhlmann, and J. F. Owens. Inclusive jet production, parton distributions, and the search for new physics. *JHEP*, 0310:046, 2003.

- [44] A. D. Martin, R. G. Roberts, W. J. Stirling, and R. S. Thorne. Uncertainties of predictions from parton distributions. i: experimental errors. *European Physical Journal C*, 28:455, 2003.
- [45] W.J.Stirling. Private communication.
- [46] R. Hamberg, W.L. van Neerven, and T. Matsuura. Drell-yan and nnlo. *Nucl. Phys. B*, 359, 2002.
- [47] The CMS Collaboration. Cms technical design report, volume ii: Physics performance. *Journal of Physics G*, 34, 2006.
- [48] H. Burkhardt and R. Schmidt. Absolute luminosity from machine parameters. LHC Project Report XX.
- [49] The ATLAS Collaboration. Atlas detector and physics performance technical design report. 1999.
- [50] The TOTEM Collaboration. Physics technical design report, 2006.
- [51] T. Junk. *Nucl. Instr. Meth.*, A 434:435, 1999.
- [52] Yongsheng Gao. Significance calculation and a new analysis method in searching for new physics at the lhc. *EPJ*, C45:659, 2006.
- [53] B. Trocmé F. Ledroit, J. Morel. Z' at lhc. ATLAS-PHYS-PUB-2006-024, 2006.
- [54] K. Sridhar Prakash Matthews, V. Ravidran. Nlo-qcd corrections to dilepton production in the randall-sundrum model. *hep-ph/050615*, 2005.
- [55] D. Acosta *et al.* Search for new physics using high mass tau pairs from 1.96-tev p anti-p collisions. *Phys. Rev. Lett*, 95, 2005.
- [56] K. Lane. *Phys. Rev.*, D 60:75007, 1999.
- [57] K. Lane and S. Mrenna. *Phys. Rev.*, D 67:115011, 2003.
- [58] K. Cheung and G. Landsberg. *Phys. Rev.*, D 62:076003, 2000.
- [59] I. Bertram *et al.* *FERMILAB-TM-2104*, 2000.